A NONLINEAR VISCOELASTIC MOONEY-RIVLIN THIN WALL MODEL FOR UNSTEADY FLOW IN STENOTIC ARTERIES

by

Xuewen Chen

A Thesis

Submitted to the Faculty

of the

WORCESTER POLYTECHNIC INSTITUTE

in partial fulfillment of the requirements for the

Degree of Master of Science

in

Applied Mathematics

by

May 2003

APPROVED:

Dr. Dalin Tang, Thesis Advisor

Dr. Bogdan Vernescu, Head of Department

Abstract

Severe stenosis may cause critical flow conditions related to artery collapse, plaque cap rupture which leads directly to stroke and heart attack. In this paper, a nonlinear viscoelastic model and a numerical method are introduced to study dynamic behaviors of the tube wall and viscous flow through a viscoelastic tube with a stenosis simulating blood flow in human carotid arteries. The Mooney-Rivlin material model is used to derive a nonlinear viscoelastic thin-wall model for the stenotic viscoelastic tube wall. The mechanical parameters in the Mooney-Rivlin model are calculated from experimental measurements. Incompressible Navier-Stokes equations in the Arbitrary Lagrangian-Eulerian formulation are used as the governing equation for the fluid flow. Interactions between fluid flow and the viscoelastic axisymmetric tube wall are handled by an incremental boundary iteration method. A Generalized Finite Differences Method (GFD) is used to solve the fluid model. The Fourth-Order Runge-Kutta method is used to deal with the viscoelastic wall model where the viscoelastic parameter is adjusted to match experimental measurements. Our result shows that viscoelasticity of tube wall causes considerable phase lag between the tube radius and input pressure. Severe stenosis causes cyclic pressure changes at the throat of the stenosis, cyclic tube compression and expansions, and shear stress change directions in the region just distal to stenosis under unsteady conditions. Results from our nonlinear viscoelastic wall model are compared with results from previous elastic wall model and experimental data. Clear improvements of our viscoelastic model over previous elastic model were found in simulating the phase lag between the pressure and wall motion as observed in experiments. Numerical solutions are compared with both stationary and dynamic experimental results. Mooney-Rivlin model with proper parameters fits the non-linear experimental stress-strain relationship of wall very well. The phase lags of tube wall motion, flow rate variations with respect to the imposed pulsating pressure are simulated well by choosing the viscoelastic parameter properly. Agreement between numerical results and experimental results is improved over the previous elastic model.

Acknowledgements

I would like to express firstly sincere thanks to my advisor Dr. Dalin Tang. His dynamic thoughts, his broad and profound knowledge, and his patient instruction have given me the greatest help in all the time of research for and writing of this thesis. Without his guidance and encouragement this master thesis would not have been possible.

I also would like to express my deep gratitude and appreciation to the faculty in Mathematical Sciences Department. I am grateful to Dr. Homer Walker, Dr. Mayer Humi, Dr. Arthur Heinricher, Dr. William Martin, Dr Christopher Larsen, and Dr. Jung-Han Kimn, from whom I have learned a lot. Thanks also go to many, many people in Mathematical sciences department, who have given me helps and cares.

My special gratitude is for my brother, Xueke Chen, for giving me his unlimited support, valuable criticisms, and all the benefits of his experience.

I dedicate this thesis to my parents Jianming Chen and Chunxiu Zhou.

Contents

List of Figures

List of Tables

Chapter 1

Introduction

Stroke and ischemic heart disease, which result from high grade stenoses, are the single most common causes of death in the United States. Approximately 35 percent of all deaths result from this cause. High grade stenoses increases flow resistance in arteries which forces the body to raise the blood pressure to maintain the necessary blood supply. Both the high pressure and the narrowing of blood vessel cause high flow velocity, high shear stress and low or negative pressure at the throat of the stenoses, low shear stress, flow separation, wall compression or even collapse at the distal side of the stenoses. These may be related to thrombus formation, atherosclerosis growth and plaque cap rupture which leads directly to stroke and heart attack. The exact mechanism of this complicated process is still not well understood. A better study in this physiological process is of great importance to early diagnosis, prevention and treatment stenoses related diseases.

A considerable number of experimental and numerical research works have been conducted to study the flow dynamics and stresses in elastic collapsible tube. Many interesting phenomena such as flow limitation, choking, flutter, and wall collapse have been identified and analyzed [1, 2, 3, 14, 15, 16, 17, 18, 19, 20, 21, 22, 33] in the last thirty years. Recently Tang [23, 24, 25, 26, 27] used axisymmetric models to investigate steady/unsteady viscous flow in elastic stenotic tubes with various stenosis stiffness and pressure conditions. Cavalcanti [28] did numerical simulation to examine the hemodynamics in a mild stenosis with consideration of pulsatile wall motion. Giddens [29] used computational methods to investigate the interaction between fluid mechanics and the artery wall. Bathe [30] introduced an axisymmetric thick-wall model with fluid-structure interactions for pulsatile blood flow through a compliant stenotic artery. Also, a different fluid-structure interactions method was developed by Yamaguchi [31] and was applied to axisymmetric and symmetric plaque models of coronary artery diseases. Ku [17] et al. conducted a series of experiments using rigid tubes, compliant tubes with rigid stenoses, thin-wall silicone tubes with stream-lined compliant stenoses and thick-wall PVA hydrogel models whose mechanical properties are close to bovine carotid arteries. Powell [32] measured the tube law for bovine carotid artery and studied the effects of severity of stenosis. Their results showed that the tube wall collapsed under physiological conditions.

While much work has been reported, the mathematical models for flow in stenotic collapsible tubes were primarily limited to 1-D models because of the difficulties in handling fluid-structure interactions with nonlinear large wall deformation, large strain and the critical flow conditions induced by the stenosis. And most research focus on elastic tubes, in which stress produces its characteristic strain instantaneously, and strain vanishes immediately on removal of the stress.

But real arteries contain a variety of tissues. When it is subjected to a constant strain, artery tissue creeps in time, and when it is subjected to a constant strain, the induced stress gradually relaxes. This transient behavior of artery is known as viscoelasticity [5] [39] [40] [46]. Some mathematical models such as Maxwell Model, Voigt Model and St. Venant Model [37] etc. have been developed to simulate the viscoelastic properties. Studies from Wesseling at al [34], Goedhard and Knoop [38] showed that the viscoelastic model with more than one time constant reflects the influence of viscoelastic properties better when representing a human artery. To better understand blood flow behavior in real arteries, a variable time constant in viscoelstic artery model may be considered.

In this thesis, firstly, the mechanical properties of artery wall are taken from Yamaguchi's experiments [41]. In experiments, the PVA hydrogel is used to make thick-walled stenosis model whose mechanical properties are very close to that of human carotid arteries. Based on the experimental data, an axisymmetric nonlinear computational model is introduced to simulate blood flow in stenotic carotid arteries. The Navier-Stokes equations are used for the fluid model. Arbitrary Lagrangian-Eulerian formulation (ALE) [42, 43, 44] is used which is suitable for problems with free moving boundaries. The SIMPLER [8] [45] algorithm based on Generalized Finite Differences with staggered grids and the upwind technique is used to solve the fluid model. A modified viscoelastic thin-wall model with variable time constant is introduced to model the dynamic nonlinear properties of the stenotic tube wall with the mechanical parameters controlled by the Mooney-Rivlin material model, which is based on the experimental measurements (Tang, 2001). An incremental boundary iteration method technique is used to handle the fluid-wall interactions. The ranges of physical parameters and geometries of the tube and fluid domain are chosen to match the experimental set-up.

Both experimental and computational results show that the viscoelasticity of tube wall causes considerable phase lag between the oscillations of downstream flow rate and imposed pressure, small phase lag between the oscillations of radius and pressure. The frequency of the oscillations is identical to that of the imposed pressure. Severe stenoses cause cyclic pressure changes between positive and negative values at the throat of the stenosis, cyclic tube compression and expansions for the axisymmetric nonlinear model and rapid shear stress changing directions in the region just distal to the stenosis which may cause excessive artery fatigue and possible plaque cap rupture. Numerical solutions are compared with experimental results and a reasonable agreement is found.

Chapter 2

Mathematical Models

2.1 The Fluid Model

We consider unsteady viscous flow in a stenotic compliant tube simulating blood flow in stenotic carotid arteries. The flow is assumed to be laminar, Newtonian, viscous, and incompressible. The shape of the tube is under zero transmural pressure and the tube wall is assumed to have no axial motion, that is, no slipping takes place between the fluid and the wall. And we also assume that there is no penetration of the fluid through the tube wall. A diagram of the experimental set-up is given in the Figure 2.1. Using Arbitrary Lagrangian-Eulerian (ALE) Formulation, the Navier-Stokes equations are given by:

$$\rho(\frac{\partial u}{\partial t}+(u-\frac{\partial X}{\partial t})\frac{\partial u}{\partial x}+(v-\frac{\partial R}{\partial t})\frac{\partial u}{\partial r}=-\frac{\partial p}{\partial x}+\mu(\frac{\partial^2 u}{\partial x^2}+\frac{\partial^2 u}{\partial r^2}+\frac{1}{r}\frac{\partial u}{\partial r}), \tag{2.1}$$

$$\rho(\frac{\partial v}{\partial t}+(u-\frac{\partial X}{\partial t})\frac{\partial v}{\partial x}+(v-\frac{\partial R}{\partial t})\frac{\partial v}{\partial r}=-\frac{\partial p}{\partial r}+\mu(\frac{\partial^2 v}{\partial x^2}+\frac{\partial^2 v}{\partial r^2}+\frac{1}{r}\frac{\partial v}{\partial r}-\frac{v}{r^2}), \tag{2.2}$$

$$\frac{\partial u}{\partial x}+\frac{v}{r}+\frac{\partial u}{\partial r}=0, \tag{2.3}$$

Where U=(u,v), u and v are the axial and radial components of the fluid velocity, ρ is density, μ is viscosity. $\frac{\partial X}{\partial t}$ and $\frac{\partial R}{\partial t}$ are velocities of the moving mesh at the position of moving mesh point considered.

To specify the shape of the tube wall (which means the inner wall, same throughout this thesis), we use $(X(t), R(X,t))$ to label the material points of the wall under zero pressure condition and $(x(X,t), r(X,t))$ to denote the position vector of the moving tube wall (to be determined). In this thesis, the tube radius under zero pressure condition is given by (see Figure 2.1)

$$R = R(X) = R_0 - S(X), \tag{2.4}$$

$$S(X) = \begin{cases} S_0 R_0 [1 - \cos(\dfrac{2\pi(X - X_1)}{X_2 - X_1})]^2 \Big/ 4, & X_1 \le X \le X_2 \\ 0, & otherwise \end{cases}, \tag{2.5}$$

Where R_0 is the radius of the uniform part of the tube, $S(X)$ specifies the shape of the stenosis, S_0 is the stenosis severity by diameter, i.e., reduction of the tube diameter caused by stenosis, X_1 and X_2 specify the beginning and ending of the stenosis. Stenosis severity is commonly defined as:

$$S_0 = \frac{(R_0 - R_{\min})}{R_0} \times 100\% . \tag{2.6}$$

For boundary conditions, we assume that no slipping and no penetration take place and the fluid and wall move together:

$$(u, v)\big|_{\Gamma} = (\frac{\partial x(X,t)}{\partial t}, \frac{\partial r(X,t)}{\partial t}) . \tag{2.7}$$

Here Γ stands for the boundary of the fluid domain bounded by the free moving tube wall,

$$x = x(X,t), r = r(X,t) = H(x,t) = H_0(x) + H_c(x,t), \tag{2.8}$$

Where $H(x,t)$ is the radius function, x is used as an independent variable in H and H_c to simplify presentation of results, $H_0(x(X)) = R(X)$ gives the resting shape of the tube, $H_c(x,t)$ gives the tube wall radial variations. At the inlet and outlet of the tube, we set:

$$p\big|_{x=0} = p_{in}(t), \tag{2.9}$$

$$p\big|_{x=l} = p_{out}(t) = const, \tag{2.10}$$

$$\frac{\partial u}{\partial x}\Big|_{x=0,l} = 0. \tag{2.11}$$

Where $p_{in}(t)$ and $p_{out}(t)$ are the pressure imposed at the inlet and outlet of the tube respectively in our experiments.

We start the computations from zero flow and zero pressure conditions with the tube taking the resting shape. The pressure at the inlet and outlet will be raised gradually to the specified pressure conditions and the model is solved until a periodic solution is obtained.

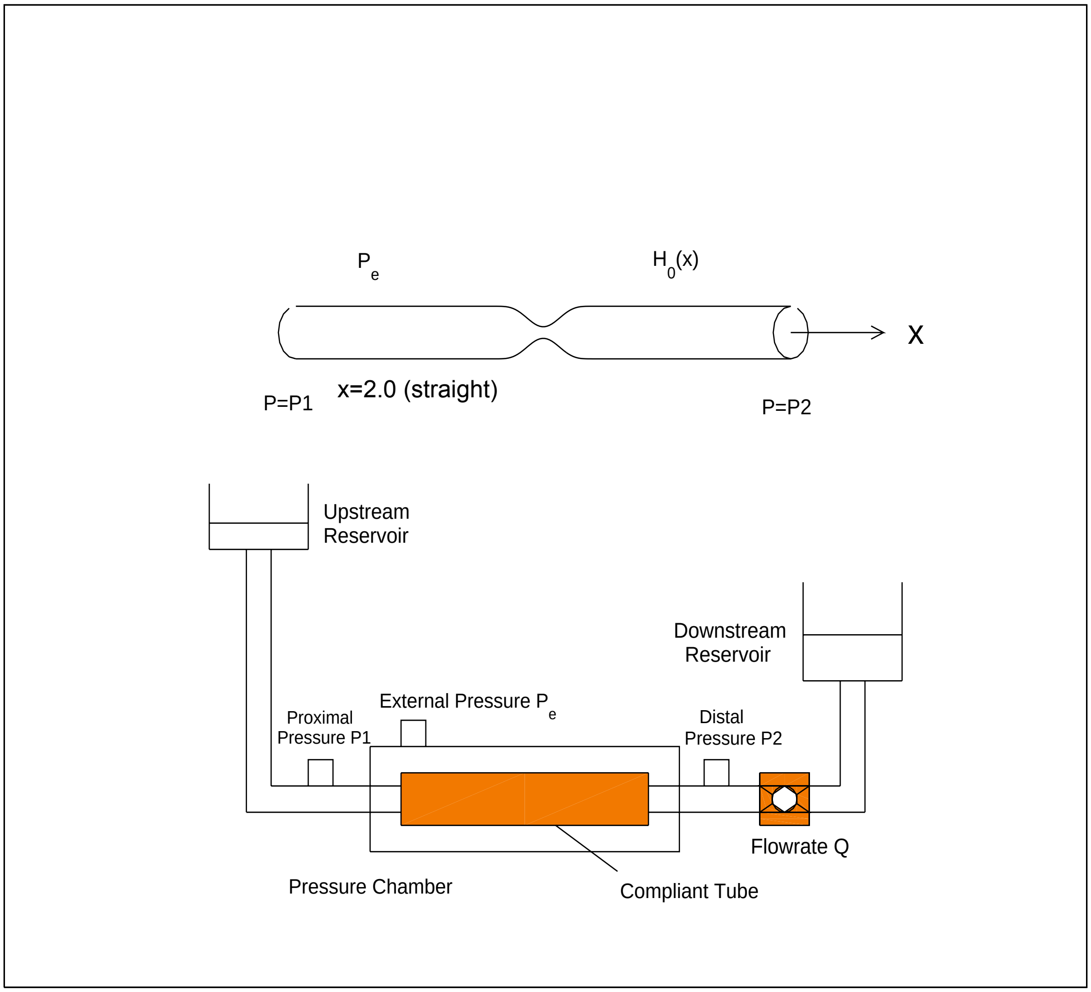

Fig. 2.1: The stenotic collapsible tube and starling resistor chamber

2.2 The Wall Model

2.2.1 Introduction

Arteries contain a variety of tissues. When it is subjected to a constant strain, artery tissue creeps in time, and when it is subjected to a constant strain, the induced stress gradually relaxes. This transient behavior of artery is known as viscoelasticity. Some mathematical models such as Maxwell Model, Voigt Model and St. Venant Model etc. have been developed to simulate the viscoelastic properties. Studies from Wesseling at al, Goedhard and Knoop showed that the viscoelastic model with more than one time constant reflects the influence of viscoelastic properties better when representing a human artery. A new idea is using a nonlinear elastic model to represent the elastic part of viscoelastic property, instead of combination of strings. So a better understand blood flow behavior in real arteries, a nonlinear model, which of course has a variable time constant, in viscoelstic artery model may be considered.

In this thesis, a nonlinear viscoelastic thin-wall model with variable time constant is introduced to model the dynamic nonlinear properties of the stenotic tube wall with the mechanical parameters controlled by the Mooney-Rivlin material model, which is based on the experimental measurements. An incremental boundary iteration method technique is used to handle the fluid-wall interactions. The ranges of physical parameters and geometries of the tube and fluid domain are chosen to match the experimental set-up.

2.2.2 Nonlinear Viscoelastic Thin-wall Model

The tube wall radial displacement is determined by the Nonlinear Viscoelastic Thin-wall Model, which is a parallel combination of a nonlinear Mooney-Rivlin (MR) string and a viscous dashpot (Figure 2.2).

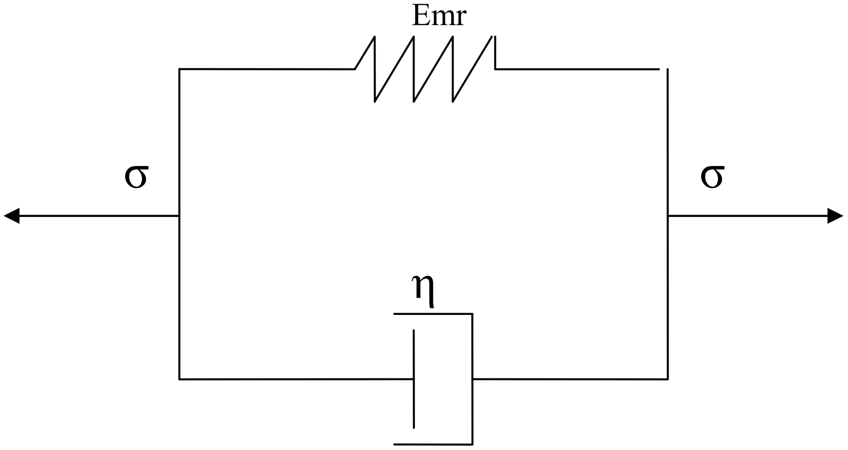

Fig. 2.2: The non-linear viscoelastic MR thin wall model.

The MR String used to describe the nonlinear material properties where the strain energy density function assumes the form:

$$W = c_1(I_1 - 3) + c_2(I_2 - 3) + D_1[e^{D_2(I_1-3)} - 1] \tag{2.1}$$

Where:

$$I_1 = \lambda^2 + 2/\lambda, I_2 = \lambda^{-2} + 2\lambda \tag{2.2}$$

are the invariants of the deformation tensor (Bathe Book, 6.27), λ is the axial stretch ratio, C_i's and D_i's are material constants. The Lagrange stress [5] of this MR string can be obtained:

$$\sigma_{MR} = C_1(2\lambda - 2\lambda^{-2}) + C_2(2 - 2\lambda^{-3}) + D_1 D_2(2\lambda - 2\lambda^{-2})e^{D_2(\lambda^2 + \frac{2}{\lambda} - 3)}, \tag{2.3}$$

where

$$\lambda = \frac{2\pi(r_0 + \delta)}{r_0} = \frac{r}{r_0}. \tag{2.4}$$

For the dashpot, stress σ_d is a function of the rate of strain multiplied by the viscous damping coefficient: η, therefore we have:

$$\sigma_d = \eta \frac{d\varepsilon}{dt}. \tag{2.5}$$

The strain can also be related to radius and thus related to stretch radio. Assuming small strains, the change in circumferential engineering strain in the artery wall is given by the change in circumference divided by the previous circumference:

$$d\varepsilon = \frac{2\pi(r + dr) - 2\pi r}{2\pi r} = \frac{dr}{r}. \tag{2.6}$$

Integrating equation (2.8) yields:

$$\varepsilon = \ln(\frac{r}{r_0}) + \varepsilon_0. \tag{2.7}$$

Here, ε and r are artery stain and radius respectively, and the subscript of 0 denotes a known condition at an initial time.

Taking the derivative of equation (2.7) with respect to time yields:

$$\frac{d\varepsilon}{dt} = \frac{1}{r}\frac{dr}{dt}. \tag{2.8}$$

If we define σ_{MR} can also be written as $\sigma_{MR} = E_{MR}\varepsilon$, where E_{MR} is the string constant of MR string, ε is the radius strain of the tube wall, then the time constant [5] of this model:

$$\zeta = \frac{E_{MR}}{\eta} \tag{2.9}$$

is obviously variable, which satisfies the discovery of Goedhard and Knoop (1973).

Combining the MR string and Dashpot, the whole stress in this model therefore is given by:

$$\sigma = \sigma_{MR} + \sigma_d \,. \tag{2.10}$$

Figure 2.3 shows the forces acting on an artery cross section. By summing the horizontal forces across the control volume, we get the circumferential stress in a thin walled cylindrical tube:

$$\sigma = \frac{pr}{h}, \tag{2.11}$$

Where h is the thickness of the artery wall and p represents the internal artery pressure, which is the same as blood pressure. Assuming the artery wall is incompressible, the volume of the wall is a constant, and we can have:

$$2\pi hr = 2\pi h_0 r_0 \,, \tag{2.12}$$

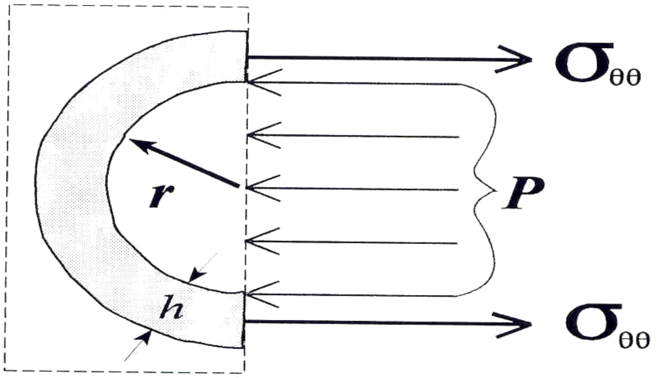

Fig. 2.3: Stress-Pressure relationship on the artery cross section.

Combining equation (2.11) and (2.12) yields an expression for the circumferential stress in an artery of incompressible material:

$$\sigma = \frac{pr^2}{h_0 r_0}, \tag{2.13}$$

Substituting equation (2.3), (2.4), (2.5), (2.8), (2.13) into (2.10) yields the Nonlinear Viscoelastic Constitutive Equation for the tube:

$$\frac{r_0(x)}{h_0(x)} p\lambda = C_1(2\lambda - 2\lambda^{-2}) + C_2(2 - 2\lambda^{-3}) + D_1 D_2(2\lambda - 2\lambda^{-2}) e^{D_2(\lambda^2 + \frac{2}{\lambda} - 3)} + \eta \frac{1}{\lambda}\frac{\partial \lambda}{\partial t}, \tag{2.14}$$

Where $\lambda = \frac{r(x,t)}{r_0(x)}$ is the stretch ratio, $C_1 = 1.0 \times 10^5 \, dyn/cm^2$, $C_1 = 1.0 \times 10^5 \, dyn/cm^2$, $D_1 = 3.8 \times 10^3 \, dyn/cm^2$, and $D_2 = 2.4$ were chosen for the artery wall to match experimental data for the bovine carotid arteries [4].

In the above equation, if we know pressure and visoelastic parameter η, initial strain ε_0, wall geometric parameters of artery r_0, h_0, initial radius $r(x,0)$, the above Nonlinear Viscoelastic Constitutive Equation for the arterial wall can be used to determine the tube radius $r(x,t)$. However, when the tube collapses, the tube is no longer adequate to determine the tube deformation, because the tube is no longer axisymmetric. A full 3-d model is needed to determine the wall deformation under collapsed condition. In this work, we assume that the tube remains axisymmetric and compresses axisymmetricly when $\frac{r_0}{r} < 1$. With this assumption, tube compression observed using this model will be a clear indication of tube collapse.

Longitudinal tension is solved from the following equilibrium equation,

$$\frac{\partial T_L}{\partial s} = -\tau , \tag{2.15}$$

where s is the arc length, τ is fluid shear stress acting on the tube wall. The initial axial stretch serves as the needed boundary condition for (2.13). The inlet and outlet of the tube are not allowed to move in the axial direction to prevent the entire tube from being pushed away by the flow. Since the tube wall is pre-stretched 36.5% and additional axial strain and displacement during the simulation are small, linear elasticity is used to determine the wall axial displacement which gives excellent approximation. Assuming the axial is linear elastic deformation, axial stress, tension and strain are related by:

$$\sigma_L = E\varepsilon_L = \frac{T_L}{h} , \tag{2.16}$$

where E is the Young's modulus which is the material physical characteristic parameter,

h is the wall thickness, σ_L and ε_L are the axial stress and strain respectively. Once the axial strain is determined, axial displacement follows easily.

Chapter 3

Numerical Method

3.1 Introduction

This model is a free moving boundary problem which involves fluid-wall interactions. The severe stenosis and viscoelasticity of the tube wall make the deformation pattern more complicated. All these require the application of multi numerical methods and techniques in this problem.

In this thesis, the conventional Arbitrary Lagrangian-Eulerian (ALE) based staggered generalized finite differences (GFD) [6] over an irregular grid with upwind differencing [7, 8] is used for the fluid model, an incremental boundary iteration technique is introduced for the fluid-wall interaction. The SIMPLER algorithm is used to solve the Navier-Stokes equations.

Using of ALE formulation enables us to choose the mesh properly to avoid large mesh distortion and eliminates the needs of interpolating the flow variables for previous steps at the new grids. GFD makes it possible for us to use finer mesh near the tube wall and in the stenotic region to handle the critical flow conditions involved in the problem. The incremental boundary iteration method is essentially a relaxation technique which is used to handle “pressure over-shooting” and “boundary over-shooting” [9, 10] and improve on the regular boundary iteration method to get convergence for this model with large strain and large deformations. Details of the numerical method are explained below.

3.2 Outline of the Numerical Method

The model is solved by using a boundary iteration method whose main steps are:

1). Start from an initial boundary, velocity and pressure.

2). In each time step,

a). Fluid Part: Using GFD to discretize the ALE Formulation and Continuity Equation, do the iterations using Simpler method till the corrections are small enough, then move to wall part.

b). Wall Part: Use the pressure and shear stress fields from the fluid part to adjust the shape of the tube by solving the viscoelatic constitutive equation of the tube wall and longitudinal equilibrium equation.

c). Repeat the fluid part and wall part until the correction:

$$\left\| f^{i} - f^{i-1} \right\| / \left\| f^{i} \right\| \leq TOL \, , \tag{3.1}$$

Where f denotes the solution vector and TOL is a specified tolerance, i.e. the computation is considered converged if the relative corrections of the variables being solved (flow velocity, pressure and wall displacement) became less than the tolerance specified.

3). Move to next time step.

Repeat above steps until a periodic solution is reached.

3.3 Generalized Finite Difference method

Generalized Finite Difference method GFD method has been used in many engineering applications where irregular geometries and free-moving boundaries are involved. The advantage of the GFD method is that the generalized finite difference schemes can be derived for arbitrary irregular grids. With the GFD method, we will be able to use finer mesh near the tube wall and in the stenotic region to handle the critical pressure and flow conditions and use coarser mesh where flow and pressure changes are less drastic. This leads to considerable reduction of grid points and CPU savings. With limited computing power, this may even be essential when we solve the corresponding model with fluid-wall interactions.

The GFD concept can be explained by the following example. To derive the second order GFD schemes for the derivatives f_x, f_r, f_{xx}, f_{rr} and f_{xr} at a given point p_0, let $X_i = (x_i, r_i)$, $(i = 1, \cdots, \text{n}, \text{n} \geq 5)$ be n neighboring points of X_0 and,

$$a_i = x_i - x_0, b_i = r_i - r_0, \rho_i = (a_i^2 + b_i^2)^{\frac{1}{2}}, f_i = f(x_i, r_i),$$

use the Taylor expansion of f at X_0 and omitting higher order terms, we have, for each X_i,

$$f_i = f_0 + a_i f_x^0 + b_i f_r^0 + \frac{1}{2}(a_i^2 f_{xx}^0 + b_i^2 f_{rr}^0 + 2a_i b_i f_{xr}^0)$$

We define:

$$A = \begin{bmatrix} a_1 & b_1 & \frac{a_1^{\ 2}}{2} & \frac{b_1^{\ 2}}{2} & a_1 b_1 \\ \cdot & \cdot & \cdot & \cdot & \cdot \\ \cdot & \cdot & \cdot & \cdot & \cdot \\ a_n & b_n & \frac{a_n^{\ 2}}{2} & \frac{b_n^{\ 2}}{2} & a_n b_n \end{bmatrix}$$

$$\overrightarrow{\Delta f} = \begin{bmatrix} f_1 - f_0 \\ \cdots \\ f_n - f_0 \end{bmatrix}$$

$$\overrightarrow{df} = \begin{bmatrix} f_x \\ f_r \\ f_{xx} \\ f_{rr} \\ f_{xr} \end{bmatrix},$$

the Taylor expansions lead to

$$A\overrightarrow{df} = \overrightarrow{\Delta f} \tag{3.2}$$

The finite difference schemes for the 5 derivatives can be obtained all at once from these equations using proper least-squares approximations. Other GFD schemes can be derived similarly.

We can get second-order scheme:

$$\overrightarrow{df} = (A^T \omega A)^{-1} A^T \omega \overrightarrow{\Delta f} = C\overrightarrow{\Delta f}, \tag{3.3}$$

where

$$\omega = \begin{bmatrix} \frac{1}{\rho_1{}^6} & & & & \\ & \frac{1}{\rho_2{}^6} & & & \\ & & \cdot & & \\ & & & \cdot & \\ & & & & \frac{1}{\rho_n{}^6} \end{bmatrix}$$

Because there are virtually no limitations on the selection of the points X_i and the derivation can be done automatically in the computer program each time the domain and mesh are adjusted, the GFD method is a suitable tool to handle the irregular geometry, non-uniform grids and the free moving boundary which requires frequent automatic re-meshing of the domain.

3.4 GFD based finite-volume method with staggered grids and upwind techniques

The finite volume method with staggered grids and upwind techniques is chosen to overcome difficulties caused by the large pressure gradient and large convection terms. GFD makes the implementation of the finite-volume method to the irregular geometry and non-uniform mesh possible. Rewriting the ALE formulation and Continuity equation into the form:

$$\rho\frac{\partial u}{\partial t}+(\rho u-\frac{\partial X}{\partial t},\rho v-\frac{\mu}{r}-\frac{\partial R}{\partial t},-\mu,-\mu,0)(u_x,u_r,u_{xx},u_{rr},u_{xr})^T+p_x=0 \quad , \qquad (3.4)$$

$$\rho\frac{\partial v}{\partial t}+(\rho u-\frac{\partial X}{\partial t},\rho v-\frac{\mu}{r}-\frac{\partial R}{\partial t},-\mu,-\mu,0)(v_x,v_r,v_{xx},v_{rr},v_{xr})^T+\frac{\mu v}{r^2}+p_r=0 \quad , \qquad (3.5)$$

$$(1,0,0,0,0)(u_x,u_r,u_{xx},u_{rr},u_{xr})^T+(0,1,0,0,0)(v_x,v_r,v_{xx},v_{rr},v_{xr})^T+\frac{v}{r}=0 \quad , \qquad (3.6)$$

for each grid point X_0, using the backward difference for the t-derivative, the generalized finite difference schemes for the space derivatives with the neighboring points chosen by the finite-volume method with staggered grids (Figure 3.1).

3.4.1 Discretization of N-S Equations over Irregular Geometry with Non-uniform Mesh

u-equation:

The location of star nodes is show in Figure 3.1; we use 8 nodes to generate the space derivatives term at u_0 in u equation, and 5 nodes to deal with convective term.

Using u_i (i=1,...8) around the star u_0, following the procedure listed above, we can get $\overrightarrow{du} = C^1 \overrightarrow{\Delta u}$. It is worth to notice that although there are convective terms in $\overrightarrow{du}$, to gain more physical meaning for our scheme, we adopt upwind scheme.

Upwind Scheme: Discretization of the Convection term at u_0

To deal with convective terms, we do not use the u_r, u_x in $\overrightarrow{du}$. Upwind method is traditional method to discretize the convection terms which is stable and provide physical meaning for the formulas.

For $u_x, u_2, u_3, u_5, u_7, u_8$ if $u \le 0$, and u_1, u_2, u_4, u_6, u_7 if $u > 0$, are used to discretize the convection terms.

For $u_r, v_1, v_2, v_3, v_4, v_5$ if $v > 0$, and v_4, v_5, v_6, v_7, v_8 if $v < 0$, used to discretize it.

By using 5 points around u_0, we can get another $\overrightarrow{du} = C^2 \overrightarrow{\Delta u}$, combining C^1 with C^2, we can get a new $\overrightarrow{du} = C\overrightarrow{\Delta u}$.

Other terms

For p_0, v_0 at u_0, we use only four points around u_0, through weight average to approximate, for p_x, v_θ, v_x, the central difference is used.

Discretizing the equation using the generalized finite difference schemes and upwind scheme, deriving and rearranging terms, we get u-equation:

$$u_0 + \sum_{i=1}^{8} k_i{}^u u_i + k_9{}^u + k_{10}{}^u (p_1{}^u - p_2{}^u) = 0, (u - equation) \tag{3.7}$$

The v equation is discretized in the same way:

$$v_0 + \sum_{i=1}^{8} k_i{}^v v_i + k_9{}^v + k_{10}{}^v (p_1{}^v - p_2{}^v) = 0, (v - equation). \tag{3.8}$$

3.4.2 Discretization of continuity equation

We discretize the continuity equation at p_0, 6 points around p_0 is used. Using the procedure of GFD, we can get

$$\sum_{i=1}^{6} k_i{}^c u_i + \sum_{i=1}^{6} k_{6+i}{}^c v_i + k_{13}{}^c = 0, (c - equation) \tag{3.9}$$

where the notations p_i, v_i at u_i are as marked in Figure 3.1. First order schemes are used for the pressure derivatives since experiences indicate that lower order schemes should be used for pressure to get better performance.

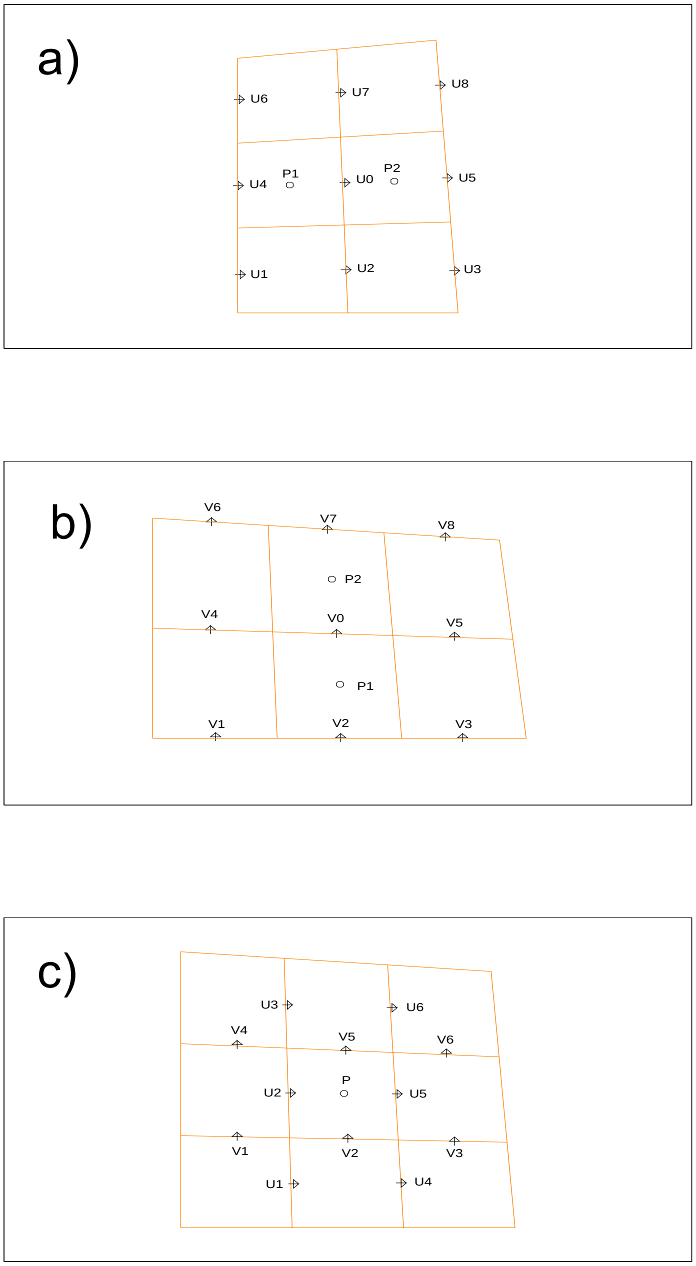

Fig. 3.1: The staggered grids and numbering of neighboring points; a) u-equation; b) v-equation; c) c-equation.

3.5 The SIMPLER Algorithm

Because the fluid-wall interaction model is very complex, we start from a well-tested SIMPLER (Semi-Implicity Method for Pressure Linked Equation) method. Instead of solving the discretized equations (3.7)-(3.9) directly, we use the SIMPLER algorithm to solve for δu and δp, the corrections to the velocity and pressure respectively [8]. By doing so, we improve on the solutions obtained from last iteration until the desired accuracy is reached. Let (u^m, v^m, p^m) be the *m*th iteration of the solutions of (3.7)-(3.9) and the residuals of (3.7)-(3.8) by (u^m, v^m, p^m) be (omitting the superscript *m*):

$$R_u(u,p) = u_0 + \sum_{i=1}^{8} k_i{}^u u_i + k_9{}^u + k_{10}{}^u (p_1{}^u - p_2{}^u),$$

$$R_v(v,p) = v_0 + \sum_{i=1}^{8} k_i{}^v v_i + k_9{}^v + k_{10}{}^v (p_1{}^v - p_2{}^v).$$

Assuming $(u+\delta u, v+\delta v, p+\delta p)$ satisfy (3.7)-(3.8), we have:

$$R_u(u+\delta u, p+\delta p) = (\delta u)_0 + \sum_{i=1}^{8} k_i{}^u \delta u_i + k_{10}{}^u (\delta p_1{}^u - \delta p_2{}^u) + R_u(u,p) = 0, \qquad (3.10)$$

$$R_v(v+\delta v, p+\delta p) = (\delta v)_0 + \sum_{i=1}^{8} k_i{}^v \delta v_i + k_{10}{}^v (\delta p_1{}^v - \delta p_2{}^v) + R_v(v,p) = 0, \qquad (3.11)$$

Neglecting $(\delta u_i, \delta v_i)$ terms in (3.10)-(3.11) leads to:

$$\delta u_0 = -R_u(u,p) - k_{10}{}^u (\delta p_1{}^u - \delta p_2{}^u), \qquad (3.12)$$

$$\delta v_0 = -R_v(v,p) - k_{10}{}^v (\delta p_1{}^v - \delta p_2{}^v). \qquad (3.13)$$

Let $(u^*, v^*) = (u+\delta u_0, v+\delta v_0)$ be the (*m+1*)th iteration and substitute it back into the equation (3.9) and using (3.12)-(3.13), δp can be determined. Then $(\delta u_0, \delta v_0)$ follows from (3.12)-(3.13) and the (*m+1*)th iteration is obtained. The above procedure is repeated until desired accuracy is reached.

3.6 4th Order Runge-Kutta Method

Nonlinear Viscoelastic Constitutive Equation for the tube:

$$\frac{\partial \lambda}{\partial t} = \left[C_1(2\lambda - 2\lambda^{-2}) + C_2(2 - 2\lambda^{-3}) + D_1 D_2(2\lambda - 2\lambda^{-2}) e^{D_2(\lambda^2 + \frac{2}{\lambda} - 3)} - \frac{r_0(x)}{h_0(x)} p\lambda \right] \frac{\lambda}{\eta}, \quad (3.14)$$

is solved by 4^{th} order explicit Runge-Kutta Method [47].

Given a general ODE:

$$\frac{dy}{dt} = f(t, y), t \geq t_0, y(t_0) = y_0, \quad (3.15)$$

The obviously approach is to integral from t_n to $t_{n+1} = t_n + h$ by using a quadrature formula:

$$y(t_{n+1}) = y(t_n) + \int_{t_n}^{t_{n+1}} f(\tau, y(\tau)) d\tau = y(t_n) + h \int_0^1 f(t_n + h\tau, y(t_n + h\tau)) d\tau,$$

and to replace the second integral by a quadrature. The outcome might have been the method:

$$y_{n+1} = y_n + h\sum_{j=1}^{\gamma} b_j f(t_n + c_j h, y(t_n + c_j h)), n = 0,1...,$$

except that we don't know the value of y at the nodes $t_n + c_1 h$, $t_n + c_2 h$, …, $t_n + c_\gamma h$. We must resort to an approximation.

We denote our approximant of $y(t_n + c_j h)$ by ξ_j, j=1, 2, …, γ. To start with, we let $c_1 = 0$, since then the approximation is already provided by the former step of the numerical method, $\xi_1 = y_n$. The idea behind explicit Runge-Kutta (ERK) methods is the express each ξ_j, j=2, 3, …, γ, by updating y_n with linear combination of $f(t_n, \xi_1)$, $f(t_n + hc_2, \xi_2)$, …, $f(t_n + hc_{j-1}, \xi_{j-1})$. Specifically, we let:

$$\begin{aligned}
\xi_1 &= y_n \\
\xi_2 &= y_n + ha_{2,1} f(t_n, \xi_1) \\
\xi_3 &= y_n + ha_{3,1} f(t_n, \xi_1) + ha_{3,2} f(t_n + c_2 h, \xi_2) \\
&\cdots\cdot \qquad (3.16) \\
\xi_\gamma &= y_n + h\sum_{i=1}^{\gamma-1} a_{\gamma,i} f(t_n + c_i h, \xi_i) \\
y_{n+1} &= y_n + h\sum_{j=1}^{\gamma} b_j f(t_n + c_j h, \xi_j)
\end{aligned}$$

The matrix $A = (a_{j,i}) j,i = 1,2,..,\gamma$, where missing elements are defined to be zero, is called the RK matrix, while

$$b = \begin{bmatrix} b_1 \\ b_2 \\ \vdots \\ b_\gamma \end{bmatrix} \text{ and } c = \begin{bmatrix} c_1 \\ c_2 \\ \vdots \\ c_\gamma \end{bmatrix}$$

are the RK weights and RK nodes respectively. We say that (3.16) has γ stages. To obtain RK matrix, the most obviously way consists of expanding everything in sight into Taylor series about (t_n, y_n), then recollect terms and compare with the Taylor Expansion of the exact solution about the same point (t_n, y_n). A great deal of persistence and care of computations are required to obtain the family of 4th order implicit Runge-Kutta method. The best-known 4th order, four-stage ERK method is:

$$A = \begin{bmatrix} & & & \\ 1/2 & & & \\ 0 & 1/2 & & \\ 0 & 0 & 1 & \end{bmatrix}, \; b = \begin{bmatrix} 1/6 \\ 1/3 \\ 1/3 \\ 1/6 \end{bmatrix}, \; c = \begin{bmatrix} 0 \\ 1/2 \\ 1/2 \\ 1 \end{bmatrix} \tag{3.17}$$

Using stretch ratio of previous time step and pressure from fluid, the Nonlinear Viscoelastic Constitutive Equation for the tube can be solved with the 4th order Runge-Kutta method during each time step. The viscoelastic coefficient in the viscoelastic constitutive equation is properly chosen to simulate well of the phase lag of tube wall motion with respect to the imposed pulsating pressure.

3.7 Incremental Boundary Iteration Method

Boundary iteration methods have become popular for solving problems with fluid-structure interactions recently where the fluid and solid models are solved iteratively until convergence is obtained. However, it has been known that the boundary iteration method may fail to converge if the tube wall is considerably compliant [11]. We use an incremental iterative method to reduce the "displacement over-shooting" and improve the convergence. Displacement over-shooting causes velocity over-adjustment at the boundary which affects the convergence of the fluid model. For a given wall adjustment $\Delta r(\theta, z)$, if the fluid model fails to converge, we reduce Δr to half and try to solve the fluid model again. This is repeated until convergence is reached. A similar relaxation technique can also be used to reduce "pressure over-shooting" which is the cause of tube wall over-adjustment. When δu and δp are obtained, we update u and p with:

$$u_{new} = u_{old} + \omega_u \delta u \,, \tag{3.18}$$

$$p_{new} = p_{old} + \omega_p \delta p \tag{3.19}$$

where ω_u and ω_p can be chosen between 0 and 1 to achieve best convergence.

3.8 Geometry and mesh

The ranges of parameters and the geometry of the tube used in the computations are chosen to match the experimental set-up [12]:

$$R_0 = 0.4cm\,,\ l = 8cm\ \textit{(tube length)},\ X_1 = 3.2cm\,,\ X_2 = 4.8cm\,,$$

$$\nu = 0.04cm^2 / s\,,\ \rho = 1g / cm^2\,,\ \nu = \mu / \rho\,. \tag{3.20}$$

The external pressure was set to zero and inlet pressure $P_{in}(t)$ and outlet pressure $P_{out}(t)$ are set to be consistent with experiments [13]. Reynolds number Re is defined as $D \cdot U / \nu$ where D is the entrance tube diameter ($2R_0$) and U is the entrance average velocity. The Reynolds number for an 80% stenosis with inlet pressure 100 mmHg and outlet pressure 20 mmHg is about 300. The units given above are used throughout this thesis.

Nun-uniform grids (Figure 3.2) were used in the computation to handle the critical flow conditions involved in the collapse process. The step size in r and x directions are reduced by fixed ratios towards the wall and the middle of the tube length to get better resolution there. The ratios are:

$$q_r = dr_{i+1} / dr_i = 0.92\,,\ q_x = dx_{i+1} / dx_i = 0.95 \tag{3.21}$$

For a ($30_r \times 100_x$) mesh, we have $dr_1 = 0.03486$, $dr_{30} = 0.00311$ at the inlet of the tube where the step size at the wall dr_{30} is less that eleventh of the starting step size dr_1. For x, we have $dx_1 = 0.21667$ at the inlet, $dx_{50} = 0.01755$ at the middle of the tube length which is less that one twelfth of dx_1. By using the non-uniform mesh, much better resolution is achieved near the wall and stenotic region with fewer grid points which lead to considerable savings of CPU time.

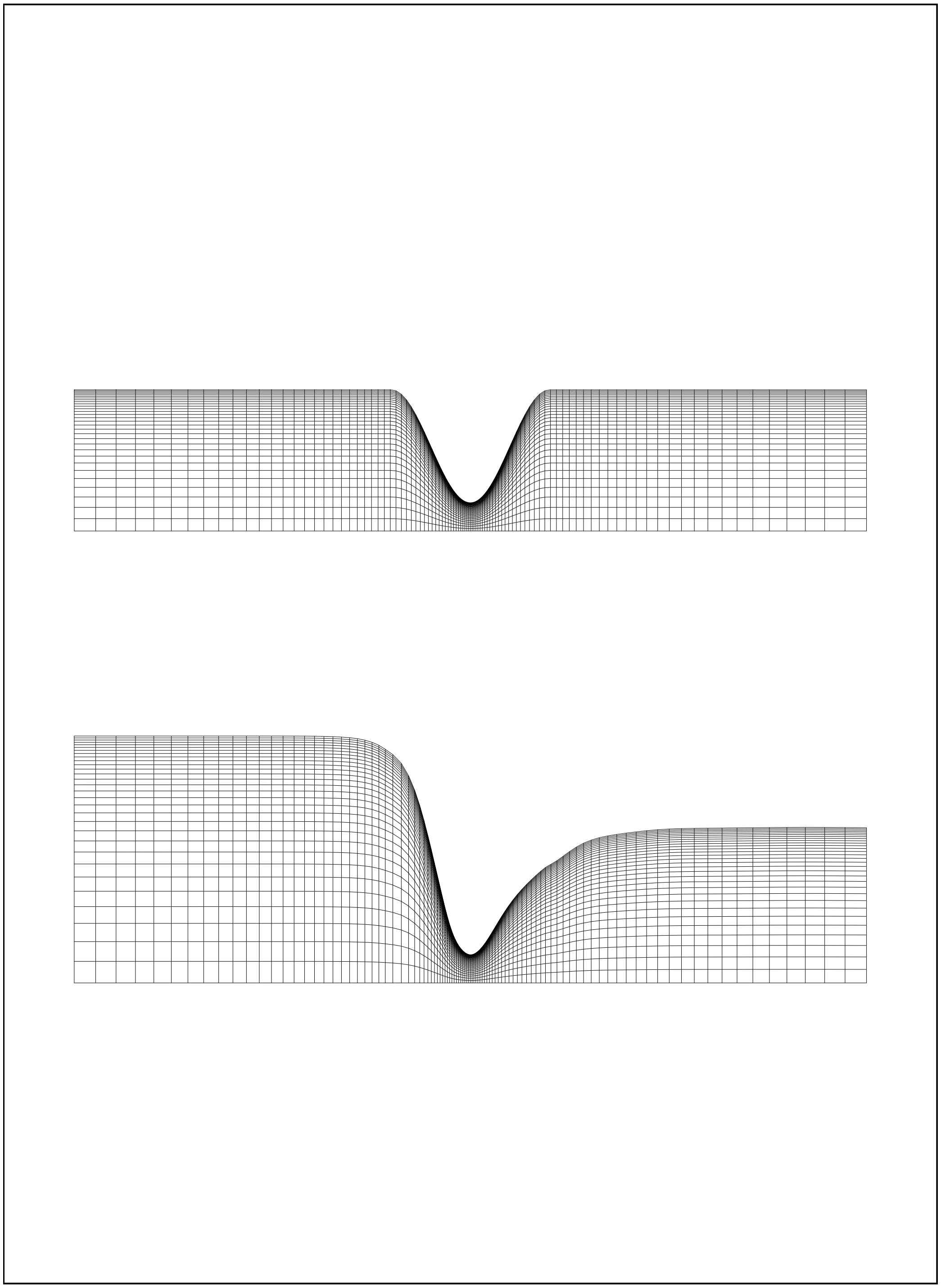

Fig. 3.2: Finer mesh is used near the tube wall and stenosis to get better resolution there.

3.9 Accuracy

Since analytic solutions for flow in a compliant stenotic tube are not available, computations are performed for flow in a rigid tube over three meshes and numerical solutions are compared with the exact solution (Fung, 1997),

$$u = -\frac{1}{4\nu}({R_0}^2 - r^2)p_x\,,\; v = 0\,,\; p_x = const\,. \tag{3.22}$$

To check the convergence of the method, Table 3.1 gives a summary of the errors which show that the algorithm converged well. The accuracy of the numerical solutions may be better than what Table 1 shows because the exact solution is assumed to be x-independent while the actual flow always has entrance and end effects.

To check the accuracy and convergence of the numerical scheme for the complaint model, three meshes were tested and the results are given in Table 3.2. While the average $dx_i \times dr_j$ is reduced about 50% from one mesh to next mesh (notice the mesh is non-uniform), the errors are reduced about 50%. This indicates that the scheme is of first order accuracy.

One may be wondering whether the remeshing, regriding and recalculation of the coefficients of the equations might affect the efficiency of the algorithm. While it does increase the complexity of the program, it actually takes very little CPU time during actual run. For the meshes used in Table 2, the CPU time for 5 equation iterations (the

SIMPLER algorithm solving (3.7)-(3.9)) were 3.27, 4.96 and 10.77 secons respectively, using an ALPHA station (500 MHz) while the CPU time for wall displacement, remeshing, regrinding and recalculation the coefficients of the equations took less than 0.01 seconds (the boundary is adjusted every 5 equation iterations).

Mesh 3 (100×30) is used for the general computations in this thesis. The tolerance for the equation iterations is set to 1.0×10^{-6}, i.e., solutions of (3.7)-(3.9) are considered obtained if the relative errors (corrections) of the velocity and pressure are less that the specified tolerance. The tolerance for the boundary iteration is set to 1.0×10^{-4}, i.e., the solution for the tube wall, flow velocity and pressure were considered “converged” for a given time step if the relative errors became less that the tolerance specified. Periodic solutions were considered obtained when the solutions started to repeat itself within 1% tolerance. Our calculations indicate that three periods are needed for the solutions to become periodic.

Mesh	$m_x \times n_r$	$e_n(u)$	$e_n(v)$	$e_n(p)$
Mesh 1	80×20	0.096	3.4×10^{-7}	3.4×10^{-6}
Mesh 2	100×30	0.032	3.3×10^{-7}	2.1×10^{-6}
Mesh 3	120×40	0.017	1.4×10^{-7}	1.0×10^{-6}

Table 3.1:

Comparison of numerical solutions with exact solution for a rigid straight tube. $p_{in} = 100mmHg$, $p_2 = 99.8mmHg$, u-max(exact)=32.98 cm/s, dt=0.005, time step computed=1600. Relative errors are defined as $e_n(f) = \|f_n - f_{exact}\|_2 / (\|f_n\|_2 + 1.0)$, n=time step.

Mesh	$m_x \times n_r$	dx_1	dx_m	dr_1	dr_n	$e_n(u)$	$e_n(v)$	$e_n(p)$	$e_n(H)$
Mesh1	70×16	0.23983	0.04193	0.04344	0.01244	9.80e-5	2.22e-4	3.57e-5	6.52e-6
Mesh2	80×20	0.22949	0.03104	0.03944	0.00809	3.68e-6	1.13e-4	9.10e-6	3.67e-6
Mesh3	100×30	0.21667	0.01755	0.03486	0.00311	3.57e-5	6.85e-5	6.57e-6	2.95e-6

Table 3.2:

Order of accuracy of the numerical method. $p_{in} = 100mmHg$, $p_2 = 30mmHg$, $S_0 = 80\%$. Step size reduction ratios are 0.92 for r and 0.95 for x. Step sizes given in the table are the max-min x-steps along the tube length and the max-min r-steps at the inlet of the tube. Relative errors are defined as $e_n(f) = \|f_n - f_{n-1}\|_2 / \|f_n\|_2$.

3.10 The parameters in Nonlinear MR viscoelastic wall model

Mechanical Parameters in MR model

The Mooney-Rivlin material model (3-22) is used to derive a nonlinear viscoelastic thin-wall model (3-33) for the stenotic viscoelastic tube wall.

$$\sigma_{MR} = C_1(2\lambda - 2\lambda^{-2}) + C_2(2 - 2\lambda^{-3}) + D_1 D_2 (2\lambda - 2\lambda^{-2}) e^{D_2(\lambda^2 + \frac{2}{\lambda} - 3)} \tag{3-22}$$

$$\frac{r_0(x)}{h_0(x)} p\lambda = C_1(2\lambda - 2\lambda^{-2}) + C_2(2 - 2\lambda^{-3}) + D_1 D_2 (2\lambda - 2\lambda^{-2}) e^{D_2(\lambda^2 + \frac{2}{\lambda} - 3)} + \eta \frac{1}{\lambda} \frac{\partial \lambda}{\partial t} \tag{3-33}$$

The mechanical parameters C_1, C_2, D_1, and D_2 in the Mooney-Rivlin model are decided from experimental measurements of stationary stress-strain relationship of artery wall:

$C_1 = 1.0 \times 10^5 dyn/cm^2$, $C_1 = 1.0 \times 10^5 dyn/cm^2$, $D_1 = 3.8 \times 10^3 dyn/cm^2$, and $D_2 = 2.4$.

Figure 3.3 comparies of pressure and stretch-ratio(λ/λ_0) relationship of artery wall between experimental data and MR model with above parameters. One can see the MR model fits the experimental data quite well.

Viscoelastic Parameter:

Once mechanical parameters in MR model are decided, the viscoelastic parameter η is adjusted so that the numerical radius under experiment pressure matches the experimental radius.

$$\eta = 20000.$$

The phase lags of tube wall motion, flow rate variations with respect to the imposed pulsating pressure are simulated well by choosing above parameters in the nonlinear MR viscoelastic wall model.

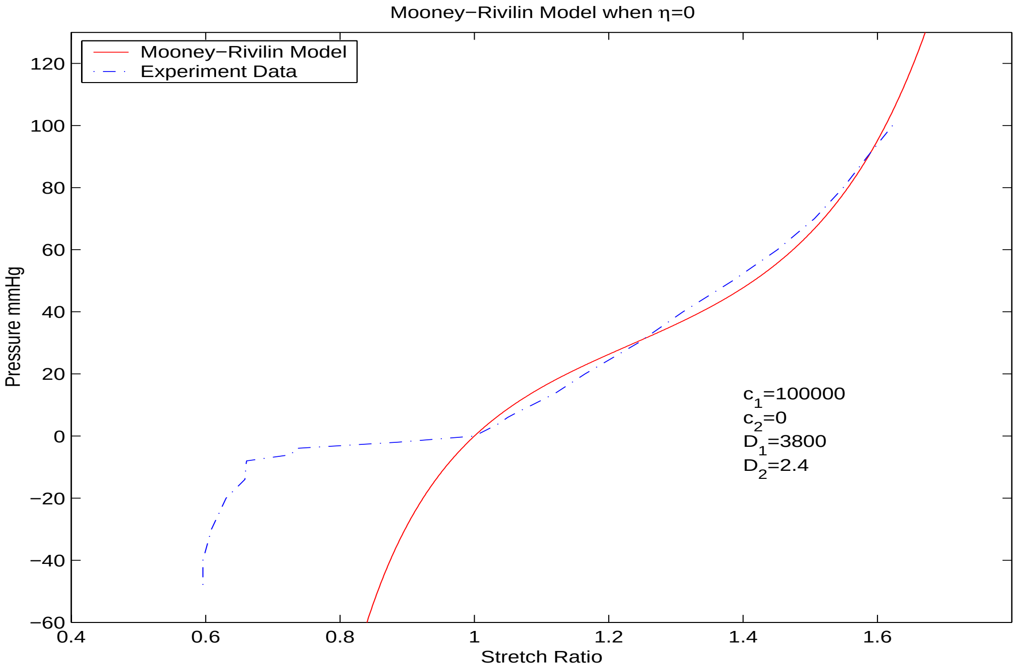

Fig. 3.3: Comparison of pressure and stretch-ratio(λ/λ_0) relationship of artery wall between experimental data and MR model.

Chapter 4

Result and Discussion

4.1 Comparison between experiment and numerical result with Elastic, Nonlinear Viscoelastic wall model

The viscoelasticity of artery wall produced a phase lag between the pressure gradient and tube radius, and between the pressure gradient and outlet flux rate. Thus if an elastic wall model is used during numerical simulation [23, 24], one can see a clear phase lag between numerical radius changing and experimental radius changing. To determine the influence of the viscoelastic properties of the tube, flows in elastic tube, viscoelastic tube are computed and compared with experiment results.

Figure 4.1.1 shows the pressure conditions imposed at the inlet and out let of the tube in the experimental. During the experiment, the inlet pressure was set to 70-130mmHg, outlet pressure was set to 5-15mmHg, and the environment pressure is set to 0 mmHg. Maximum inlet pressure occurs at 189°. The same pressure condition is used in the numerical simulation.

Figure 3.3 shows Mooney-Rivlin material model with $C_1 = 100{,}000 dyn/cm^2$, $C_2 = 0$, $D_1 = 3800 dyn/cm^2$, $D_2 = 2.4$ fits the mechanical property of tube wall quite well. The stress-stretch ratio λ/λ_0 relation of the tube tested in a uniaxial tensile loading condition. It is worth noting the Mooney-Rivlin model can not fit the experimental data well when the load condition is less than zero. This is because we assumed the tube is still axisymmetric when it collapses under negative pressure, but in reality, we don't have enough information about the changing of stress-stretch ratio under negative loading. Actually the experimental data is not totally reliable in this case because of the measuring difficulty.

Figure 4.1.2 plots the numerical and experimental radius changing at x=2.0cm in a tube with stenosis 80% during one period. The maximum radius in experiment occurs at $\theta = 205.2^{\circ}$. Maximum numerical radius from elastic wall model occurs at $\theta = 187.2^{\circ}$.

Figure 4.1.3 shows by using non-linear MR viscoelastic wall model with $\eta = 20000$, the maximum numerical radius occurs at $\theta = 201.5^{\circ}$. The phase difference between maximum numerical radius and experimental observation is reduced 79.44% by using viscoelastic MR wall model instead of elastic wall model. The phases lag simulation between input pressure and wall motion is improved 88.27% by using viscoelastic MR Model.

Figure 4.1.4 shows the comparison of tube numerical radius with elastic model, viscoelastic MR model and experiment results at x=2.0 cm during one period. A phase lag between elastic numerical radius variation and experimental radius variation is canceled by using viscoelastic MR wall model.

Figure 4.1.5 gives the elastic computational and experimental flow rates at the outlet during one period. While there is a rough agreement, one can see that there again has a clear phase shift between computational and experimental data.

Figure 4.1.6 shows the comparison between the numerical flow rate from the non-linear viscoelastic MR wall model and experimental result at a period. This indicates that the phase lag in Fig. 10 is caused by viscoelastic properties of the tube wall and can be decreased by viscoelastic MR wall model.

Figure 4.1.7 plots the numerical flow rates and experimental result in the same figure to give a better description of the effects of viscoelasity of tube wall.

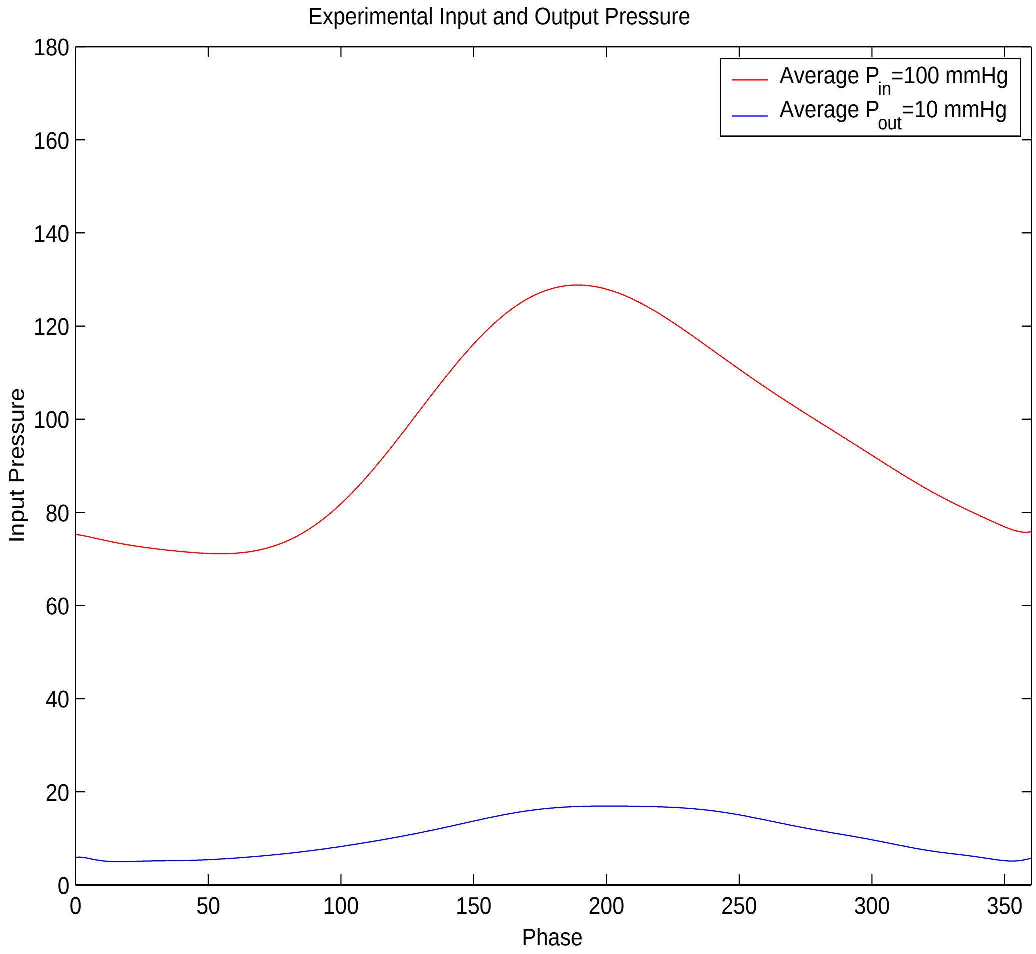

Fig. 4.1.1: The experimental pressure conditions imposed at the inlet and outlet of the tube, $p_{in} = 70 - 130 mmHg$, $p_{out} = 5 - 15 mmHg$

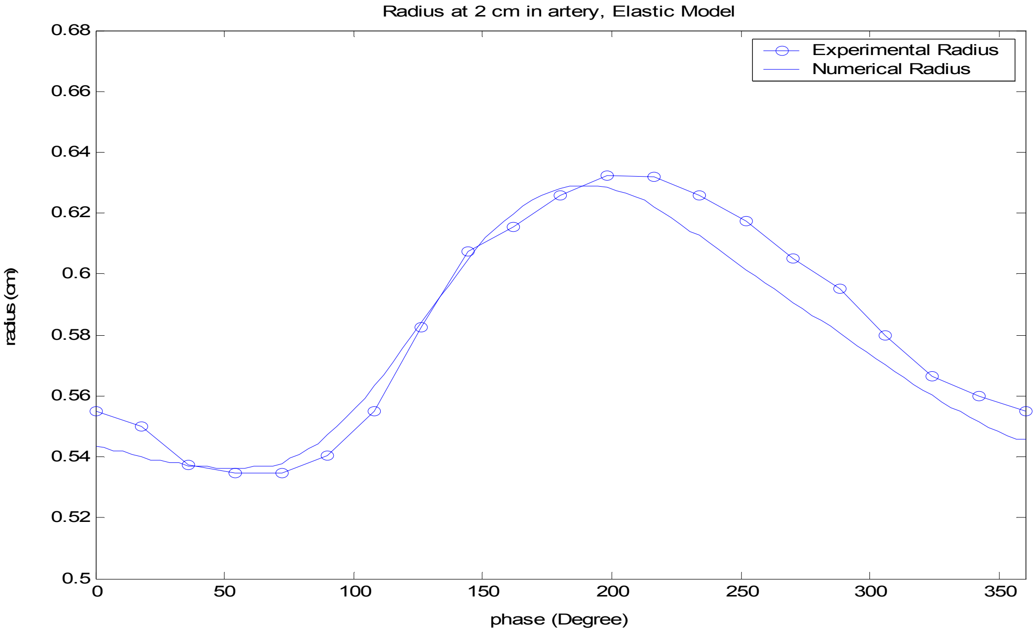

Fig. 4.1.2 Comparison of tube radius between numerical elastic wall model and experiment results at x=2.0 cm. $S_0 = 80\%$, $p_{in} = 70 - 130 mmHg$, $p_{out} = 5 - 10 mmHg$.

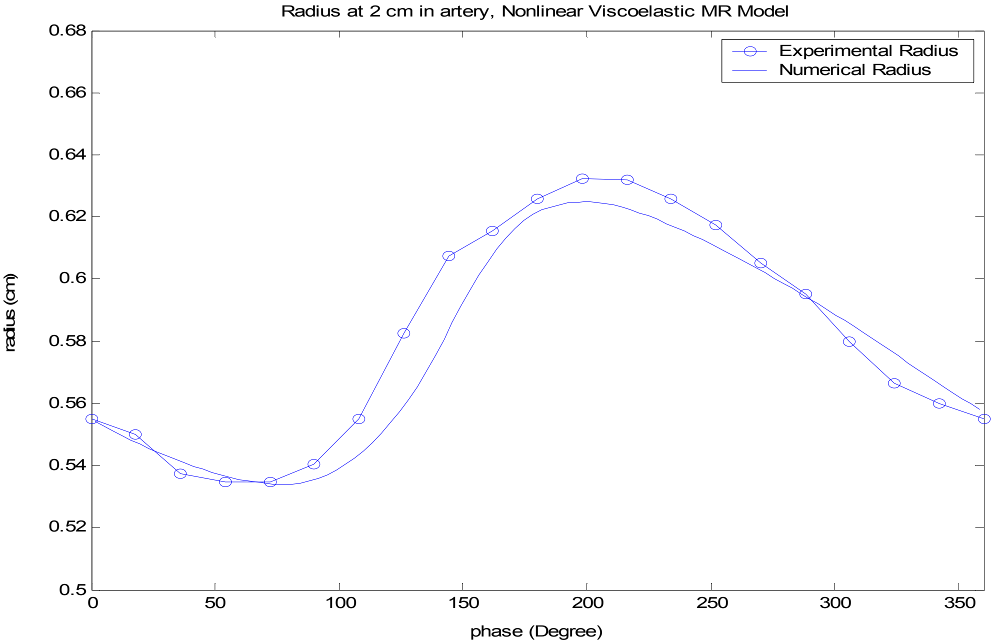

Fig. 4.1.3: Comparison of tube radius between numerical MR viscoelastic wall model and experiment results at x=2.0 cm. $S_0 = 80\%$, $p_{in} = 70 - 130 mmHg$, $p_{out} = 5 - 10 mmHg$.

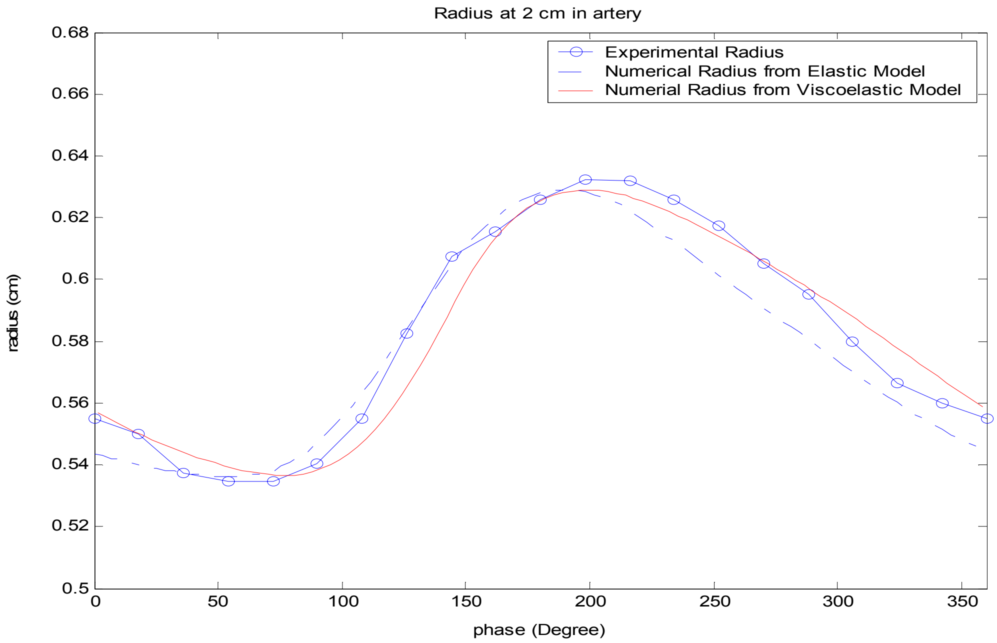

Fig. 4.1.4: Comparison of tube numerical radius and experiment results at x=2.0 cm. $S_0 = 80\%$, $p_{in} = 70 - 130mmHg$, $p_{out} = 5 - 10mmHg$.

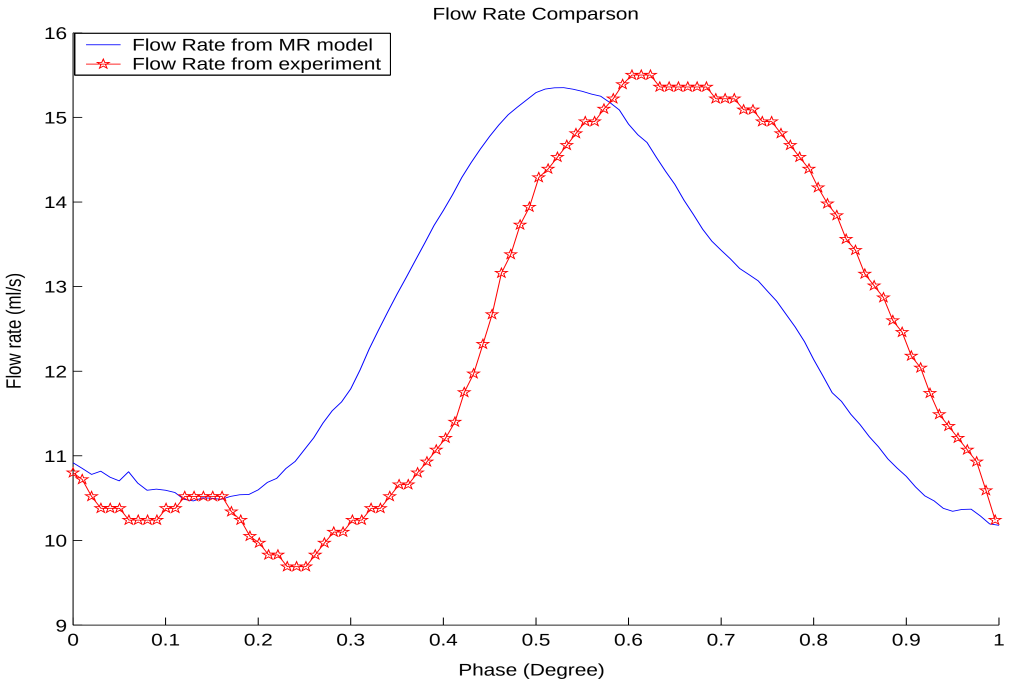

Fig. 4.1.5: Comparison of numerical flow rate from elastic wall model and experiment results at a period. $S_0 = 80\%$, $p_{in} = 70 - 130mmHg$, $p_{out} = 5 - 10mmHg$.

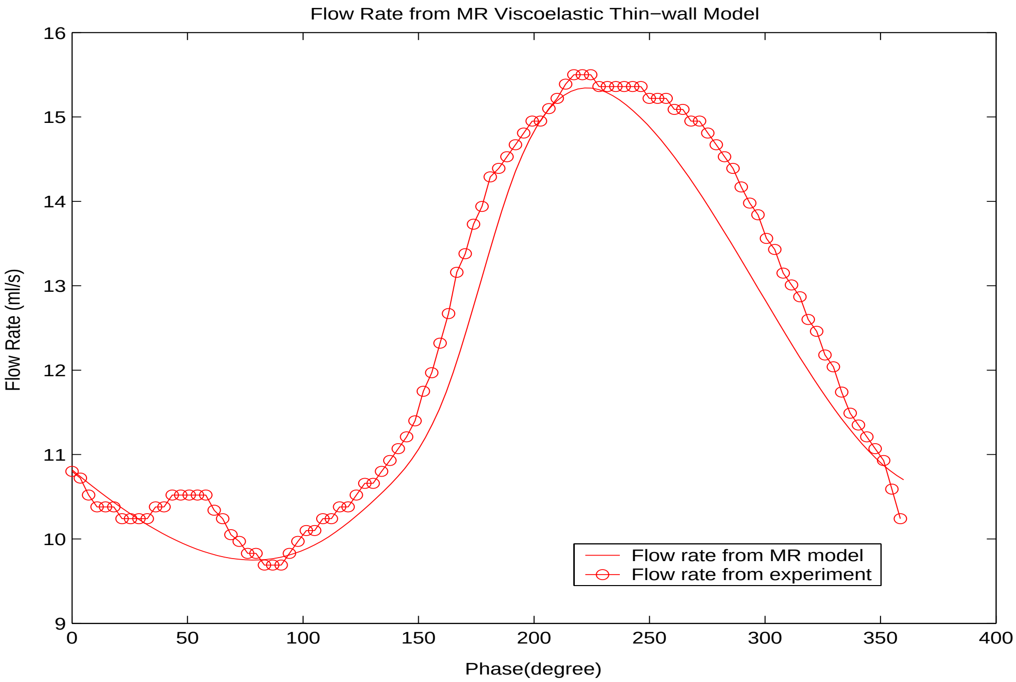

Fig. 4.1.6: Comparison of numerical flow rate from MR viscoelastic wall model and experiment results at a period. $S_0 = 80\%$, $p_{in} = 70 - 130mmHg$, $p_{out} = 5 - 10mmHg$.

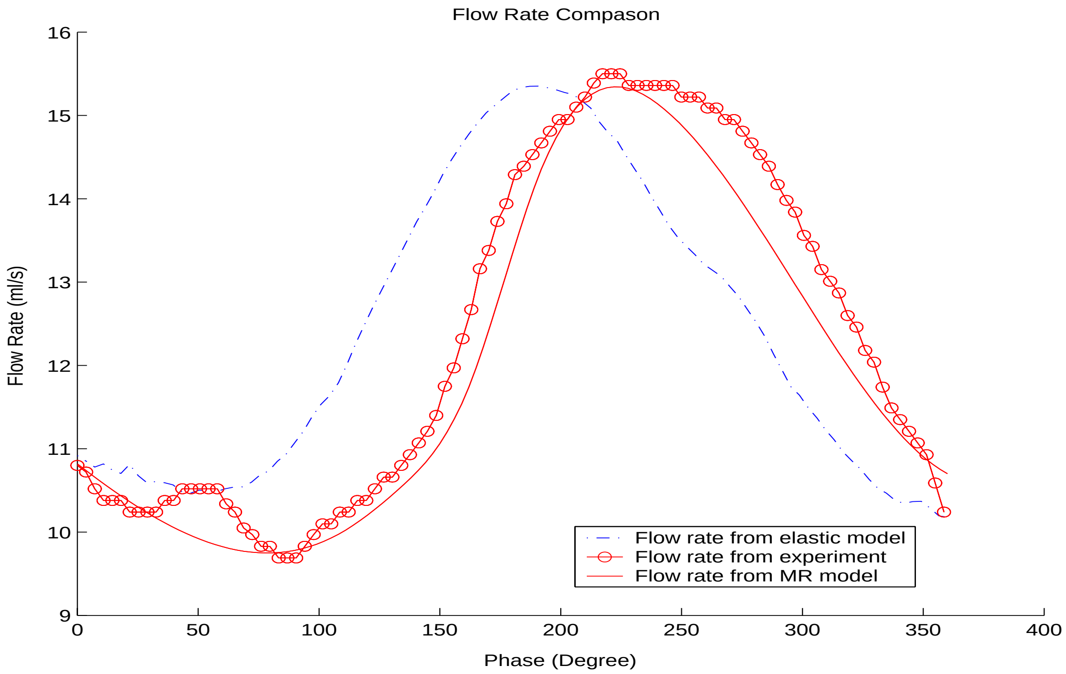

Fig. 4.1.7: Comparison of numerical flow rate and experiment results at a period. $S_0 = 80\%$, $p_{in} = 70 - 130 mmHg$, $p_{out} = 5 - 10 mmHg$.

4.2 Comparison the effect of normal pressure condition and high pressure condition

To see the influence of the imposed pulsatile pressure on the flow and wall behaviors, the pressure imposed in the inlet of the tube (P_{in}) was set to $70 \sim 130mmHg$ and $90 \sim 150mmHg$, representing high and normal pressures; the pressure imposed in the outlet of the tube (P_{out}) was set to $10mmHg$. Stenosis is still 80% by diameter. Comparison of the two cases is also included in the following figures.

Figure 4.2.1 plots the transmural pressures along the tube wall on the high pressure and normal pressure cases. It is observed that in both cases, minimum pressures occurred at the tube at the throat of the stenosis, and the axial location of the minimum pressure for the $Pin_{\max}$s are shifted slightly because the tube is pushed more to the downstream side by the flow.

a). Normal pressure: $P_{in} = 70 \sim 130mmHg$, the minimum pressures are –8.36 and -22.79 mmHg;

b). High pressure: $P_{in} = 90 \sim 150mmHg$, the minimum pressures are -10.87 and -26.49 mmHg.

Figure 4.2.2 plots the wall compression distal to the stenosis under high pressure with that under normal pressure. High pressure cause more tube wall compression, cyclic wall compression caused by the high pressure is more noticeable that that from the normal case. This indicates that high pressure is more likely to causes cyclic wall compression which leads to accelerated artery fatigue.

Figure 4.2.3 plots the stress distribution on the wall for these two cases, maximum shear stress for the high pressure case is much more greater that that for the normal pressure case. High shear stress more likely cause cap rupture which leads directly to stroke and heart attack.

Figure 4.2.4 plots the behavior of axial maximum velocity under these two prescribed inlet pressure conditions during one period. High pressure causes
high velocity which is more likely to cause rupture.

Figure 4.2.5 plots the behavior of the minimum pressure under these two prescribed inlet pressure conditions during one period. Minimum pressure under high pressure condition is obviously less than that under normal pressure condition.

a). Normal Pressure

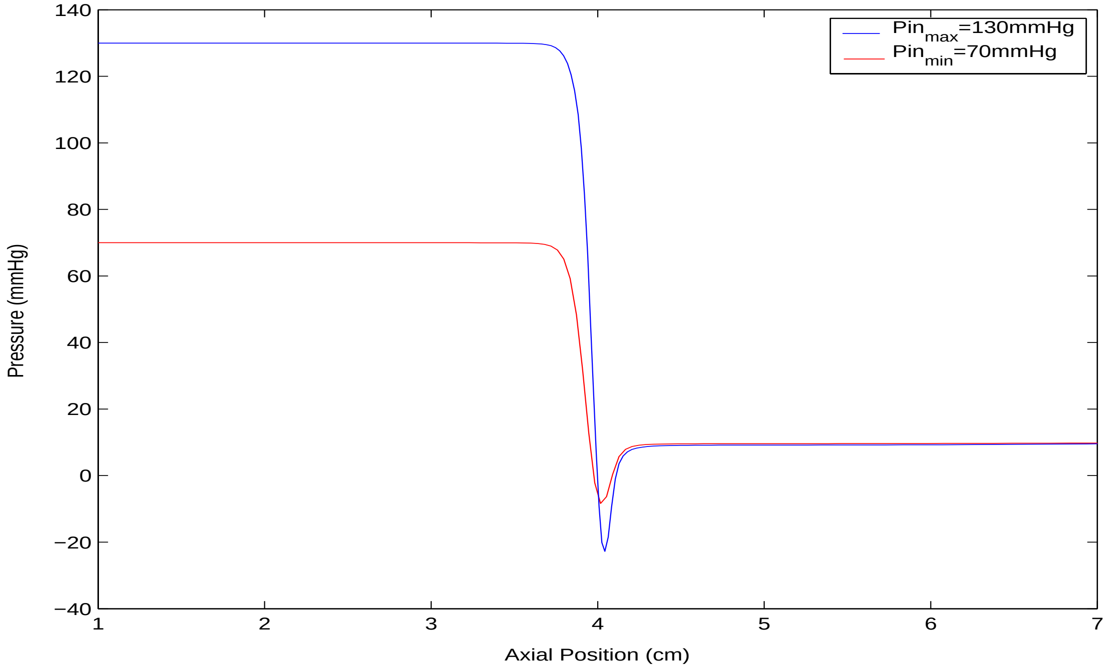

b). High Pressure

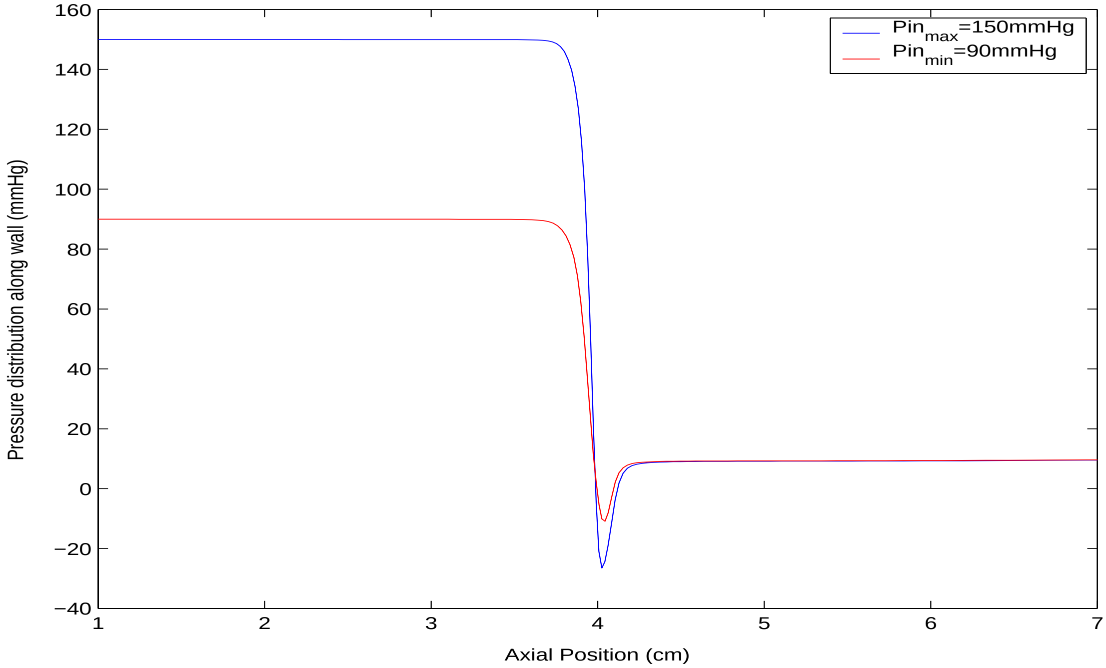

Fig. 4.2.1: Comparison of transmural pressure under prescribed inlet pressure conditions, High pressure cause more negative pressure. a) Normal Pressure: P_{in} =70~130 mmHg; b) High pressure: 90~150mmHg.

a). Normal Pressure

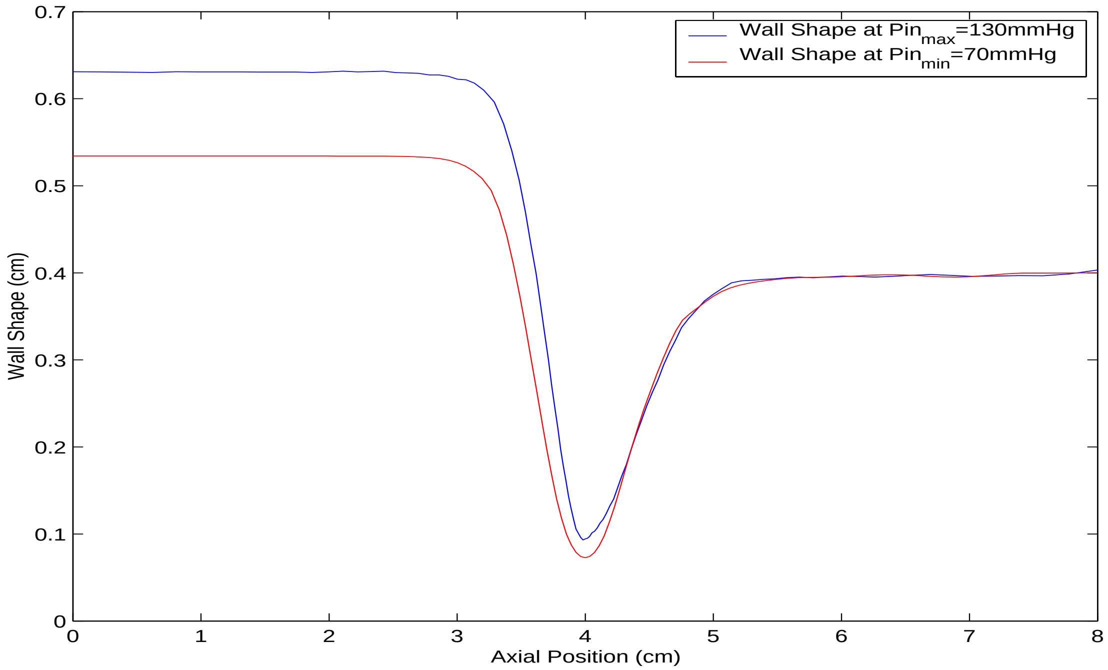

b). High Pressure

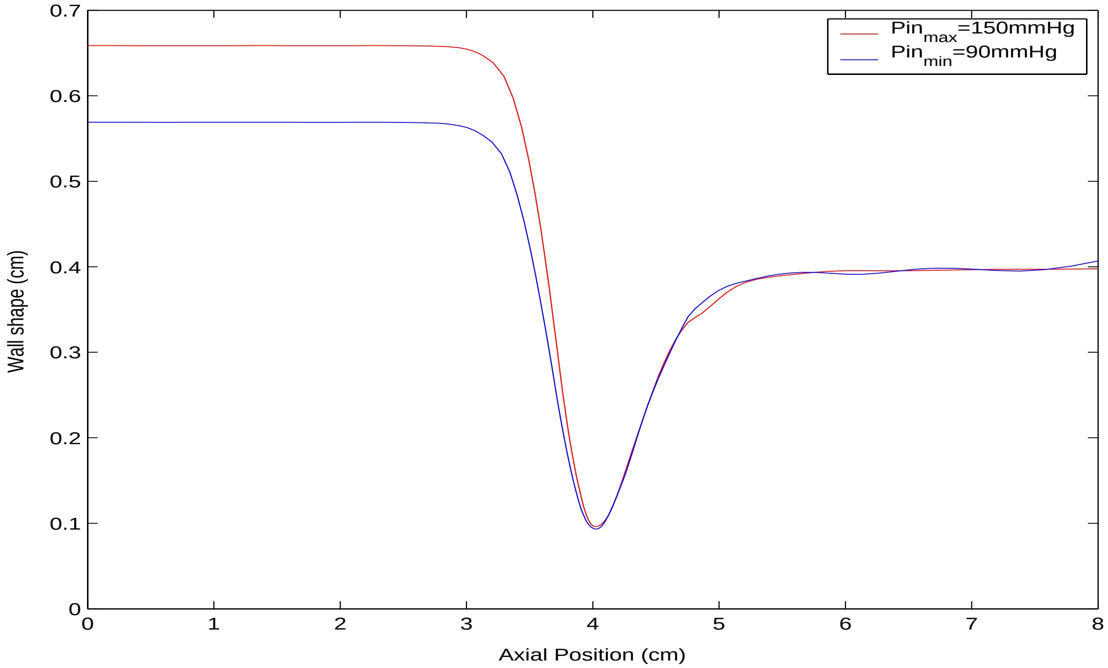

Fig. 4.2.2: Tube wall radius curves under two prescribed inlet pressure conditions. Higher pressure caused more tube wall compresssion. $S_0 = 80\%$; Pout=10 mmHg; axial pre-stretch=36.5%. a) Normal pressure: $Pin = 70 \sim 130 mmHg$; b) High pressure: $Pin = 90 \sim 150 mmHg$.

a). Normal Pressure

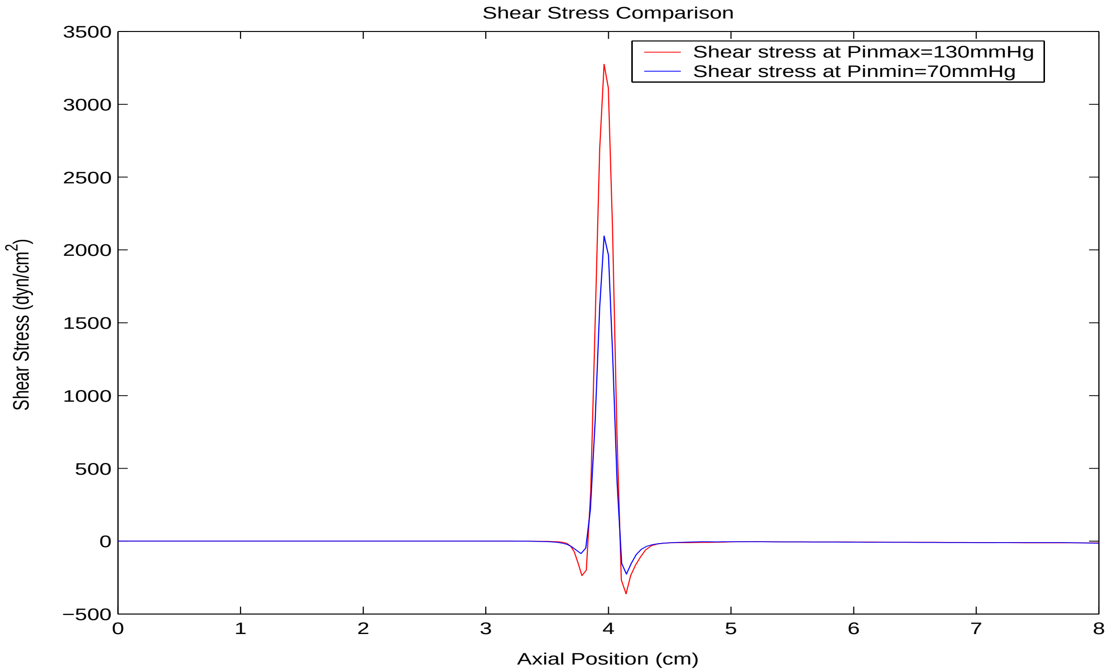

b). High Pressure

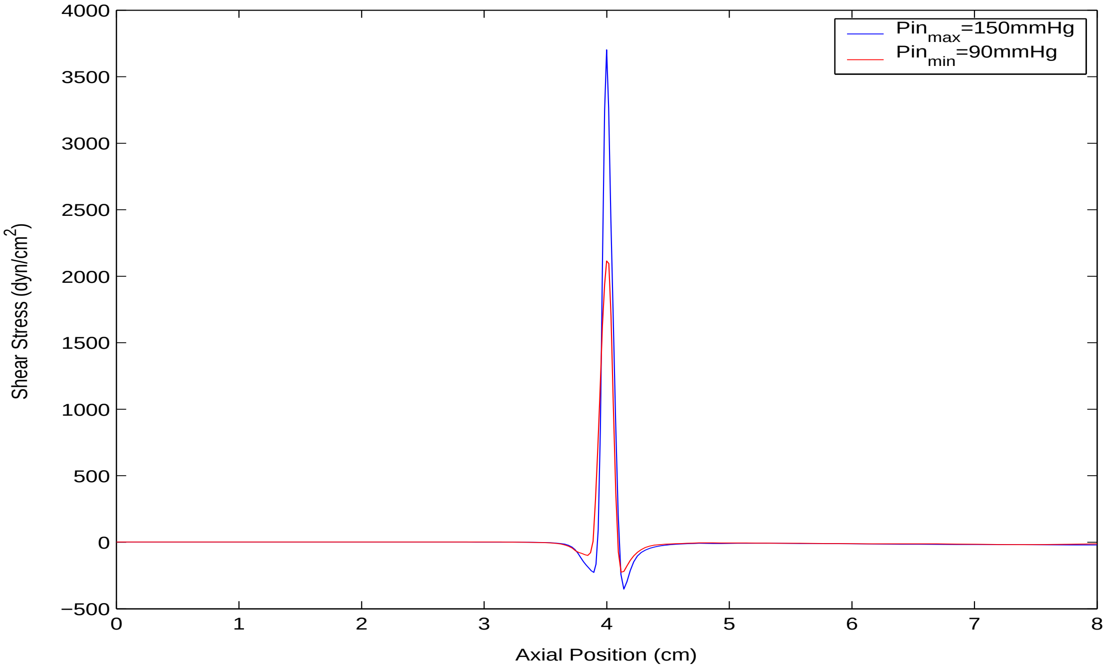

Fig. 4.2.3: Comparison of shear stress on the wall (dyn/cm^2) under maximum and minimum inlet pressure conditions, $S_0 = 80\%$; Pout=10 mmHg; axial pre-stretch=36.5%. a) Normal pressure: $Pin = 70 \sim 130 mmHg$; b) High pressure: $Pin = 90 \sim 150 mmHg$.

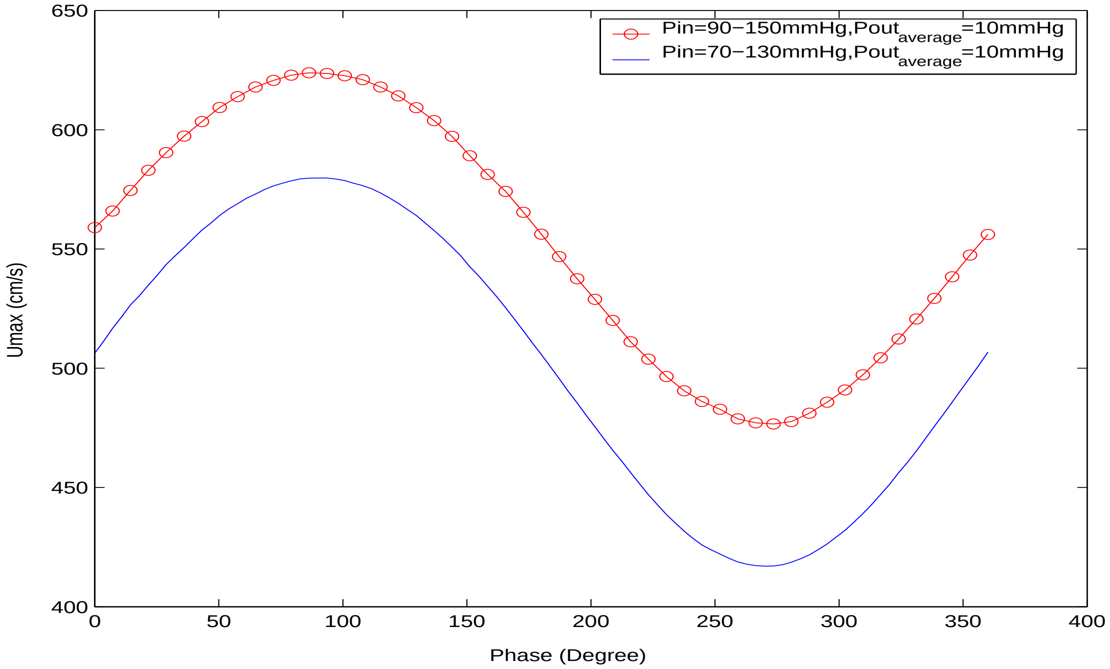

Fig. 4.2.4: Comparison of maximum axial velocity under unsteady inlet pressure conditions. $S_0 = 80\%$; Pout=10 mmHg; axial pre-stretch=36.5%.

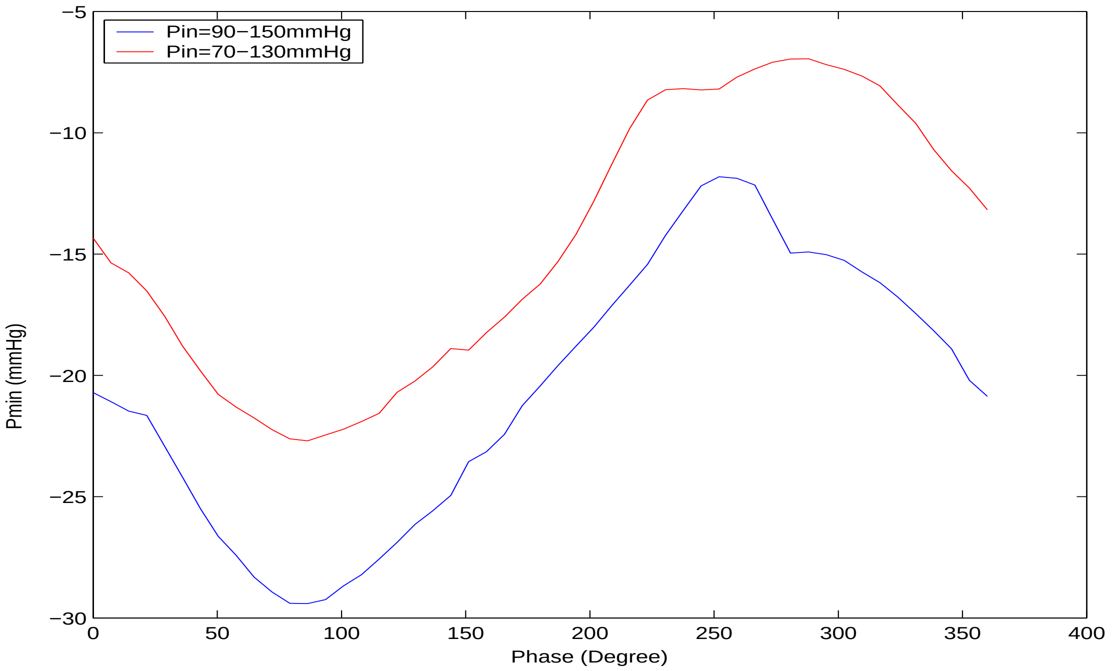

Fig. 4.2.5: Comparison of minimum pressure under unsteady inlet pressure conditions. $S_0 = 80\%$; Pout=10 mmHg; axial pre-stretch=36.5%.

4.3 Comparison the effect of severity of stenosis on the tube wall

Since pressure decreases considerably when passing a severe stenosis, the effect of the stenosis severity on flow and pressure fields becomes much more noticeable when comparison is made with flow rate fixed. Two cases are designed to compare the effct of severity of stenosis on the tube wall:

- Severity 50%, inlet pressure: 70~130 mmHg, outlet pressure: 68.6~128.6 mmHg.
- Severity 80%, inlet pressure: 70~130 mmHg, outlet pressure: 10 mmHg.

Figure 4.3.1 plots the transmural pressures along the tube wall on S0=80% and S0=50% cases. It is observed that in both cases, minimum pressures occurred at the tube at the throat of the stenosis too. And the negative pressure for the high severity case S0=80% is -22.79 mmHg when the imposed pressure conditions are: Pin=130 mmHg and Pout=10 mmHg, while no negative pressure is observed for S0=50% case when imposed pressure conditions are: Pin=130 mmHg and Pout=10mmHg.

Figure 4.3.2 plots the wall compression under high severity of stenosis with that under normal severity. One can observe that normal stenosis will not affect the shape of the tube, while high severity stenosis cause more tube wall compression.

Figure 4.3.3 plots the shear stress distribution on the wall for the two cases. We can conclude that high stenosis cause much greater shear stress which is more likely to cause cap rupture and leads directly to stroke and heart break.

- S0=80%: Max shear stress=3273.9 dyn/cm^2;
- S0=50%: Max shear stress=76.1 dyn/cm^2.

Figure 4.3.4 plots the behavior of the minimum pressure under these two prescribed inlet pressure conditions and stenosis severity conditions during one period. Minimum pressure under high stenosis severity condition is all negative during the period.

Figure 4.3.5 plots the behavior of axial maximum velocity under these two prescribed inlet pressure conditions and stenosis severity conditions during one period. High stenosis causes larger velocity which is more likely to cause rupture.

These indicate that when the same flow rate is maintained, severe stenosis cause considerable negative pressure and high shear stress in the tube while milder stenosis has very little effect on the pressure filed and shear stress. This explains why mild stenosis in the artery will not affect the function of artery and can be regarded as health.

a) S0=80%

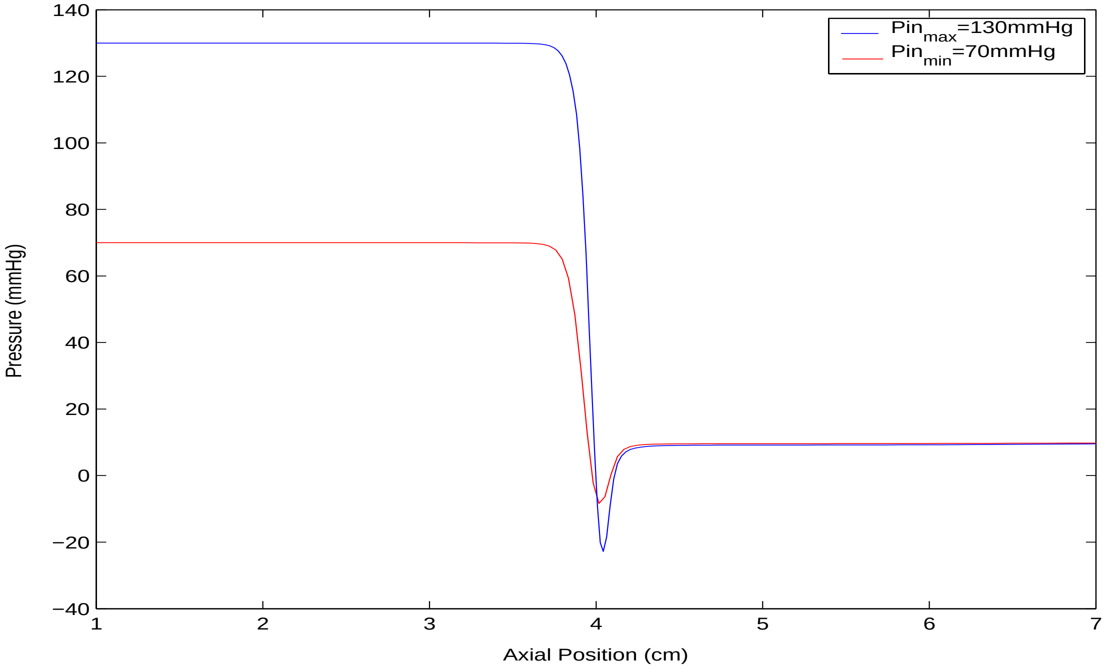

b) S0=50%

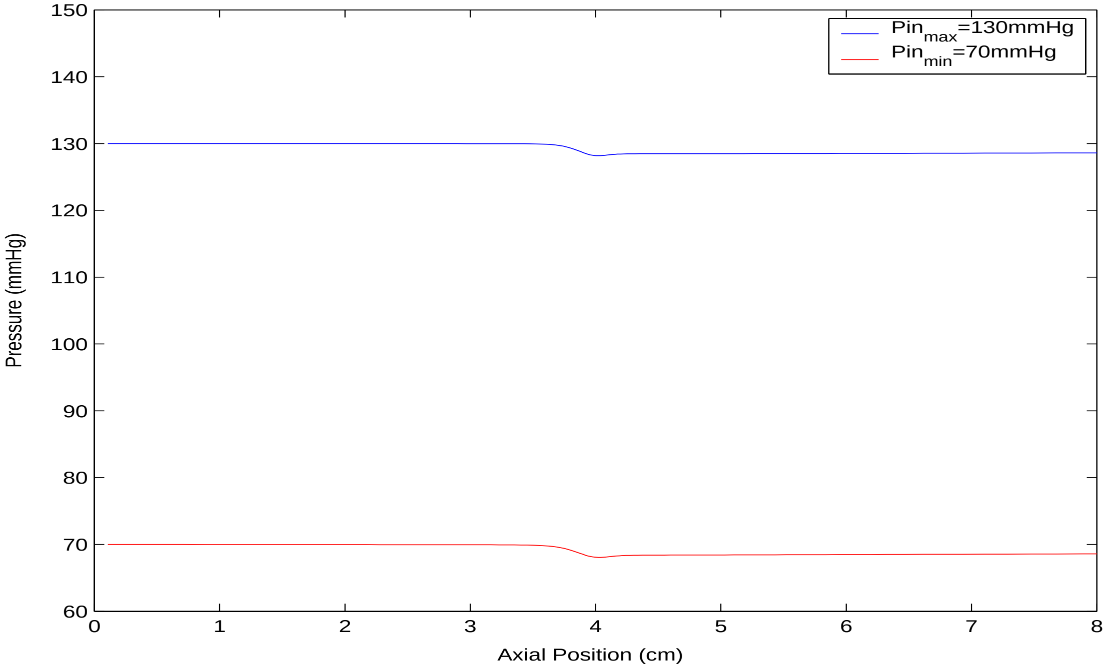

Fig. 4.3.1: Comparison of transmural pressure under different stonosis severity conditions. . a) $S_0 = 80\%$, $Pin = 70 \sim 130mmHg$; $Pout = 10mmHg$; b) $S_0 = 50\%$, $Pin = 70 \sim 130mmHg$; $Pout = 68.6 \sim 128.6mmHg$.

a) S0=80%

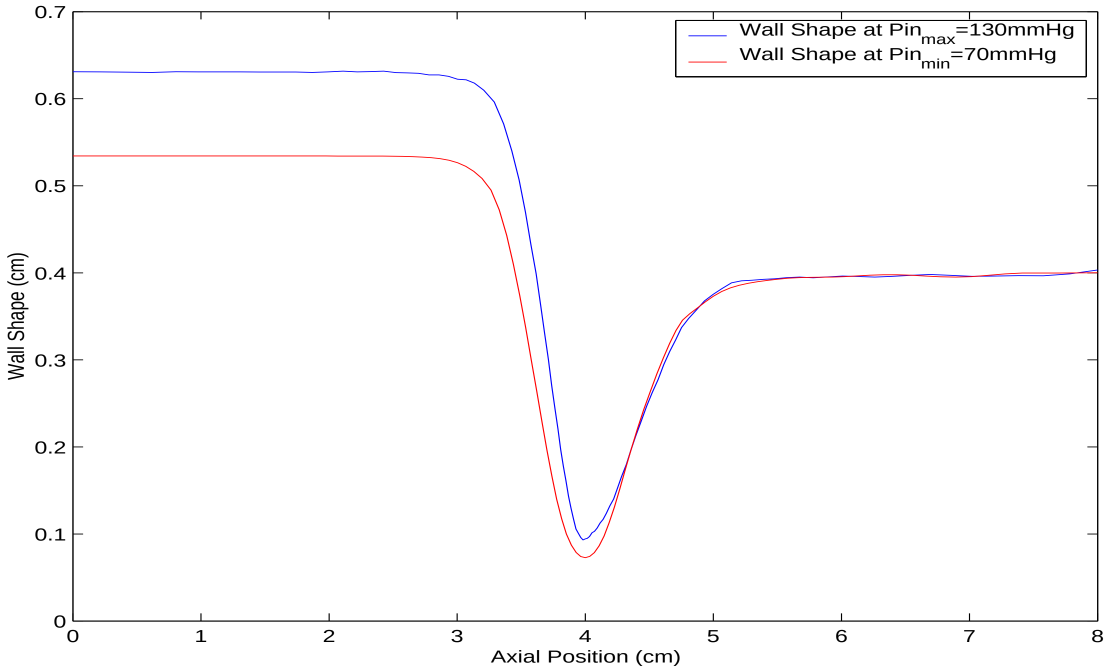

b) S0=50%

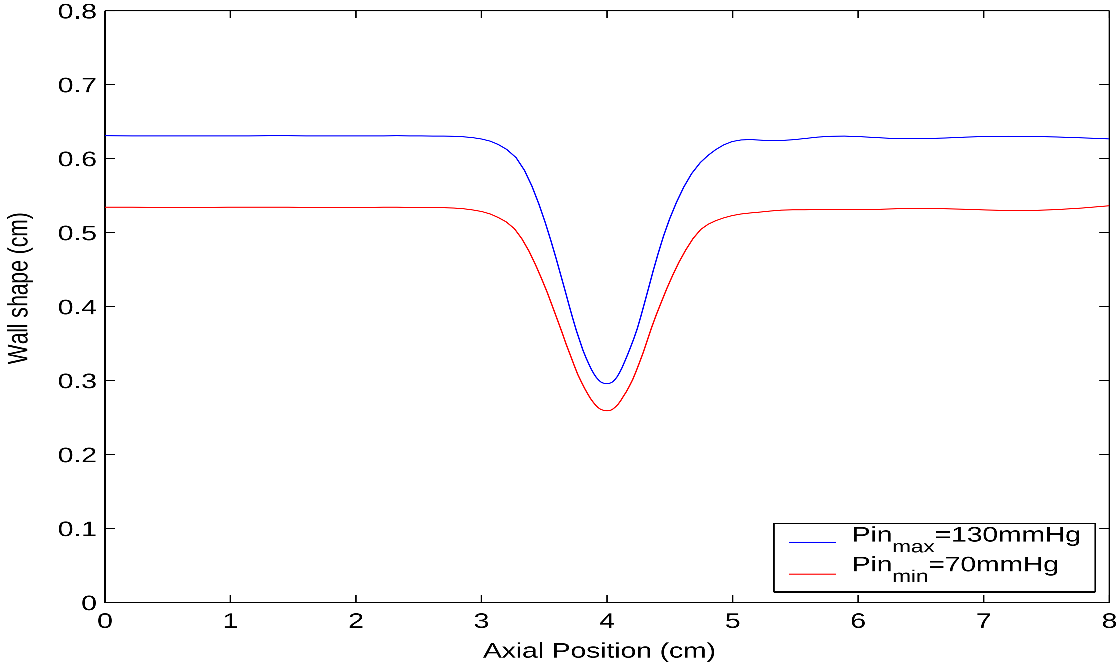

Fig. 4.3.2: Plots of tube wall radius curve under different stenosis severity condtions. . a) $S_0 = 80\%$, $Pin = 70 \sim 130mmHg$; $Pout = 10mmHg$; b) $S_0 = 50\%$, $Pin = 70 \sim 130mmHg$; $Pout = 68.6 \sim 128.6mmHg$.

a) S0=80%

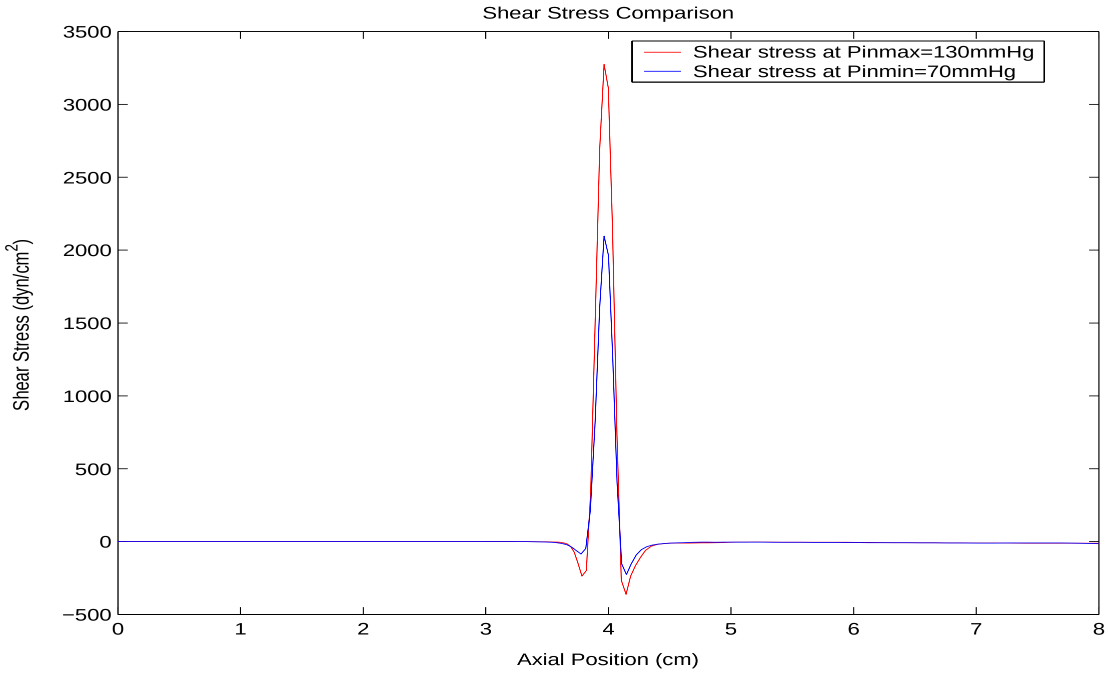

b) S0=50%

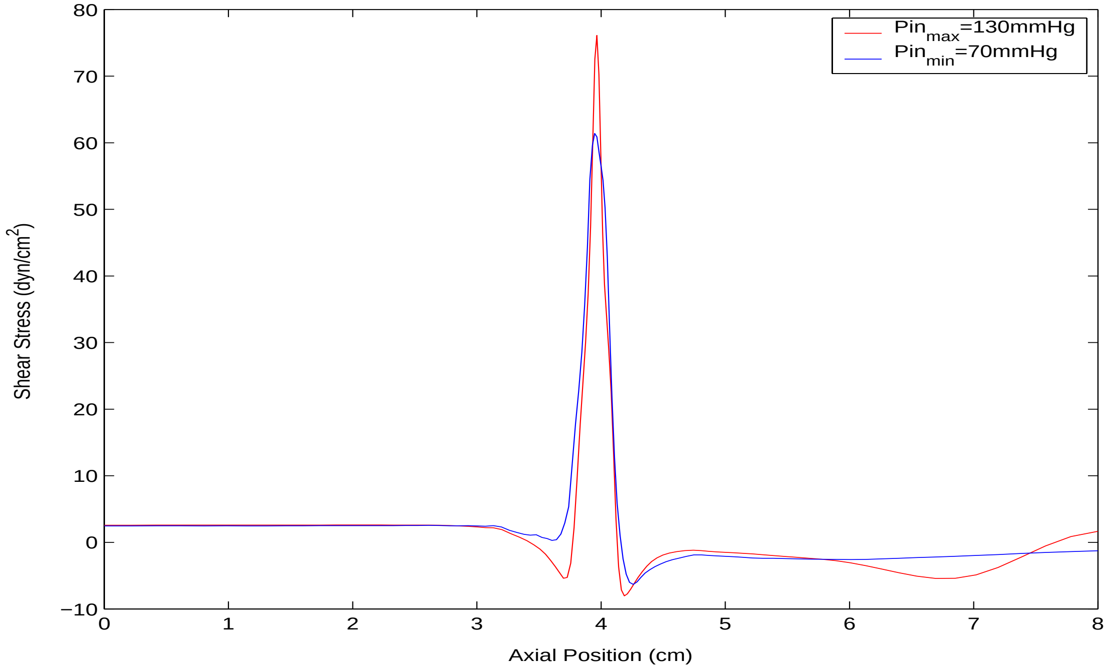

Fig. 4.3.3: Comparison of shear stress on the wall (dyn/cm^2) under different stenosis severity conditions imposed to maximum and minimum inlet pressure conditions. a) $S_0 = 80\%$, $Pin = 70 \sim 130mmHg$; $Pout = 10mmHg$; b) $S_0 = 50\%$, $Pin = 70 \sim 130mmHg$; $Pout = 68.6 \sim 128.6mmHg$.

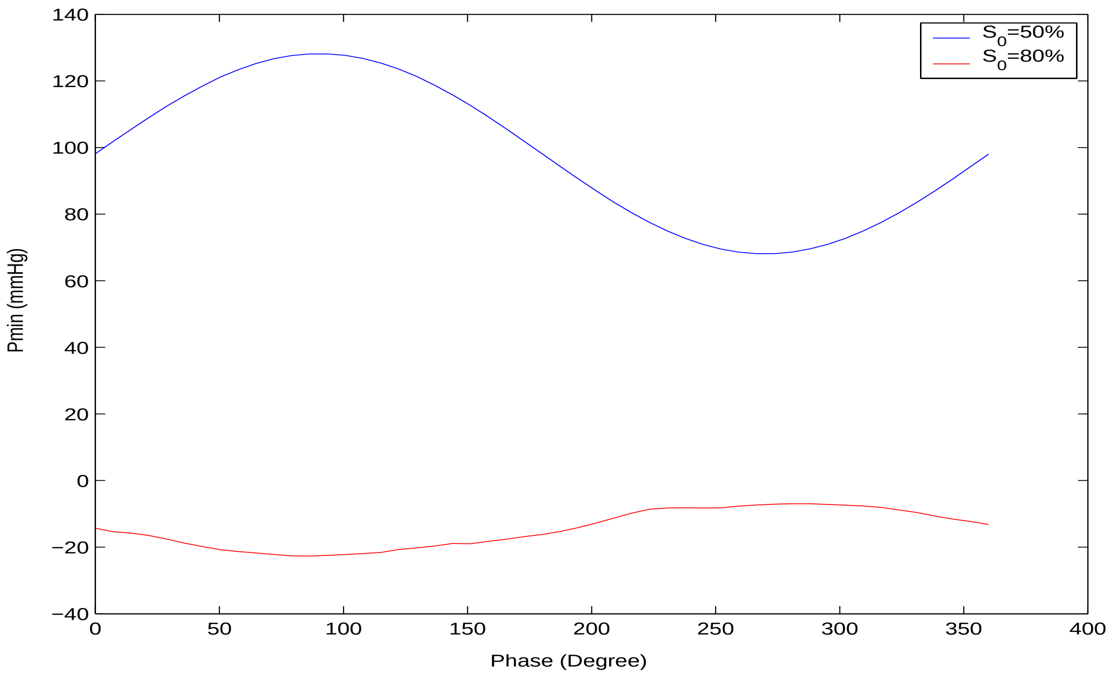

Fig. 4.3.4: Comparison of minimum pressure Pmin under different stenosis severity conditions. Inlet and outlet pressure imposed on S0=50% tube: $S_0 = 80\%$, $Pin = 70 \sim 130mmHg$; $Pout = 10mmHg$; Inlet and outlet pressure imposed on S0=80% tube: $S_0 = 50\%$, $Pin = 70 \sim 130mmHg$; $Pout = 68.6 \sim 128.6mmHg$.

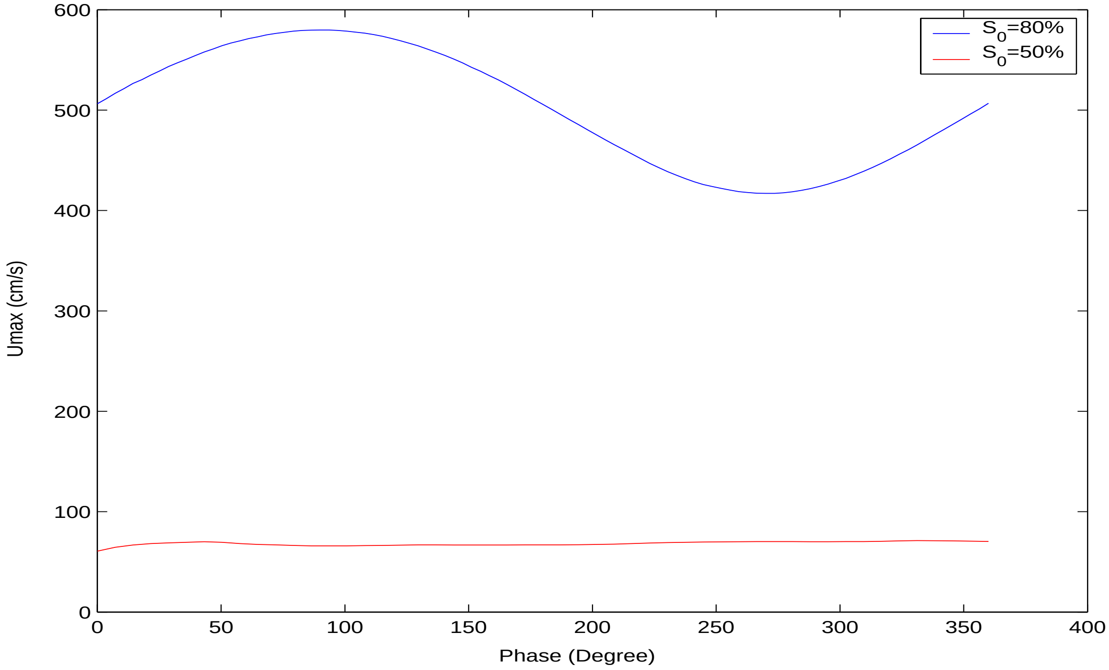

Fig. 4.3.5: Comparison of maximum velocity Umax under different stenosis severity conditions. Inlet and outlet pressure imposed on S0=50% tube: $S_0 = 80\%$, $Pin = 70 \sim 130 mmHg$; $Pout = 10 mmHg$; Inlet and outlet pressure imposed on S0=80% tube: $S_0 = 50\%$, $Pin = 70 \sim 130 mmHg$; $Pout = 68.6 \sim 128.6 mmHg$.

Chapter 5

Conclusion

A nonlinear viscoelastic model and a numerical method are introduced to study dynamic behaviors of the tube wall and viscous flow through a viscoelastic tube with a stenosis simulating blood flow in human carotid arteries. The Mooney-Rivlin material model is used to derive a nonlinear viscoelastic thin-wall model for the stenotic viscoelastic tube wall. The mechanical parameters in the Mooney-Rivlin model are calculated from experimental measurements. Interactions between fluid flow and the viscoelastic axisymmetric tube wall are handled by an incremental boundary iteration method. Clear improvements (88.27%) of our viscoelastic model over previous elastic model were found in simulating the phase lag between the pressure and wall motion as observed in experiments. Our result shows that viscoelasticity of tube wall causes considerable phase lag between the tube radius and input pressure. Severe stenosis causes cyclic pressure changes at the throat of the stenosis, cyclic tube compression and expansions, and shear stress change directions in the region just distal to stenosis under unsteady conditions. Numerical solutions are compared with experimental results and a reasonable agreement is found.

Bibliography

1. C. D. Bertram, Unstable equilibrium behavior in collapsible tubes, J. Biomech., 19 (1986) 61-69.
2. R. W. Brower and C. Scholten, Experimental evidence on the mechanism for the instability of flow in collapsible vessels, Med. Biol. Eng., 13, (1975), 839-845.
3. D. Elad, D. Katz, E. Kimmel and S. Einav, Numerical schemes for unsteady fluid flow through collapsible tubes, J. Biomed. Engng., Vol 13, (1991), 10-18.
4. D. Tang, C. Yang, S. Kobayashi, and D.N. Ku, Steady flow and wall compression in stenotic arteries: a 3-D thick-wall model with fluid-wall interatctions, J. Biomech. Engng. Vol. 123, (2001), 548-557.
5. Y.C. Fung, Biomechanics, Mechanical properties of living tissues, second edition, Prentice Hall, New Jersey, 1993.
6. T. Liszka, J. Orkisz, The Finite difference method at arbitrary irregular grids and its application in applied mechanics, Computers and Structures, Vol. 11, (1980), 83-95
7. A. N. Brooks and T. J.R. Hughes, Streamline upwind/Petrov-Galerkin formulations for convection dominated flows with particular emphasis on the incompressible Navier-Stokes Equations, Com. Meth. in Applied Mech. and Engng., Vol. 32, (1982), 199-259.
8. S. V. Patankar, Numerical heat transfer and fluid flow, Taylor & Francis Publishers, 1980.
9. Bathe KJ., Finite element procedures, Prentice Hall 1996.

10. Rugonyi S, BatheKJ., On finite element analysis of fluid flows fully coupled with structural interactions. CMES 2001; 2(2): 195-212.

11. ADINA R & D, Inc., 1999, ADINA System 7.3 release Notes.

12. D. N. Ku, S. Kobayashi, D. M. Wootton and D. tang, Compression from dynamic pressure conditions in models of arterial disease, Annals of Biomed, Engng., Vol. 25, supp. 1, (1997), S-22.

13. S. Kobayashi, D. Tang, and D. N. Ku, Pulsatile flow through a stenotic collapsible tube, Proc. of the 76th JSME Fall Annu. Meeting, (1998), 265-266.

14. M. Heil and T. J. Pedley, Large axisymmetric deformation of a cylindrical shell, J. Fluids and Structures, Vol. 9, (1995), 237-256.

15. M. Heil and T. J. Pedley, Large post-buckling deformations of cylindrical shells conveying viscous flow, J. Fluids and Structures, Vol. 10, (1996), 565-599.

16. R. D. Kamm and A. H. Shapiro, Unsteady Flow in a collapsible tube subjected to external pressure or body force, J. Biomech. Engng., Vol. 95, (1979), 1-78.

17. D. N. Ku, M. N. Zeigler, R. L. Binns and M. T. Stewart, A study of predicted and experimental wall collapse in models of highly stenotic arteries, Proc. 2nd Intl Symp on Biofluid Mechanics and Biorheology, D. Liepsch, ed., (1989), 409-416.

18. D. N. Ku, M. N. Zeigler, and J. M. Downing, One-dimensional steady inviscid flow through a stenotic collapsible tube, J. Biomech. Engng., Vol. 112, (1990), 444-450.

19. M. E. Rosar, A three-dimensional computer model for fluid flow through a collapsible tube, Ph.D Thesis, New Yourk University, 1995.

20. M. E. Rosar, Fluid flow in elastic tubes: A three-dimensional, immersed boundary

numerical model, Proc. of the Third World Congress of Biomech., (1998), 35.

21. A. H. Shapiro, Steady flow in collapsible tubes, J. of Biomech. Engng., Vol. 99, (1977), 126-147.

22. N. Stergiopulos, J. E. Moore, Jr., A. Strassle, D. N. Ku and J. J. Meister, Steady flow test and demonstration of collapse on models of compliant axisymmetric stenoses, Advances in Bioengineering, ASME BED-Vol. 26, (1993), 455-458.

23. D. Tang, Numerical solutions of viscous flow in elastic tubes with stenoses of various stiffness, Proceedings of the 1995 Bioengineering Conference, (1995) 521-522.

24. D. Tang, An axisymmetric model for viscous flow in tapered collapsible stenotic elastic tubes, 1996 Advances in Bioengineering, BED-Vol. 33, pp. 87-88, 1996.

25. D. Tang, C. Yang, S. Kobayashi, and D. N. Ku, Negative transmural pressure and a new collapse criterion for viscous flows in stenotic collapsible tubes, Abstracts of the 19th Annual Meeting of CAMS, pp. 71-72, 1998.

26. D. Tang, D. Anderson, S. Biz and D. N. Ku, Steady viscous flow in constricted elastic tubes subjected to a uniform external pressure, Int'1 J. for Num. Meth in Engng., Vol. 41, (1998), 1391-1415.

27. D. Tang, C. Yang, and D. N. Ku, A 3-D thin-wall model with fluid-structure interactions for blood flow in carotid arteries with symmetric and asymmetric stenoses, Computers and Structures, Vol. 72, (1999), 357-377.

28. S. Cavalcanti S., Hemodynamics of an artery with mild stenosis, J. Biomechanics, Vol. 48, No. 4, pp. 387-399, 1995.

29. M. D. Deshpande, D. P. Giddens, and R. F. Mabon, Steady laminar flow through

modeled vascular stenoses, J. Biomechanics, 9, pp. 165-174, 1976.

30. M. Bathe, A fluid-structure interaction finite element analysis of pulsatile blood flow through a compliant stenotic artery, B. S. Thesis, MIT, 1998.

31. T. Yamaguchi, T. Kobayashi, and H. Liu, Fluid-wall interactions in the collapse and ablation of atheromatous plaque in coronary arteries, Proceedings of the Third World Congress of Biomechanics, pp. 20, 1998.

32. Powell B. E., Experimental measurements of Flow through stenotic collapsible tubes, M. S. Thesis, Georgia Inst. Of Tech., 1991.

33. D. Tang, C. Yang, H. Walker, S. Kobayashi, and D. N. Ku, Simulating cyclic artery compression using a 3-D unisteady model with fluid-structure interactions. Computer and Structures, Vol. 80 (2002), 1651-1665.

34. K. L. Wesseling, H. Weber, B. De Wit, Estimated Five component viscoelastic Model Parameters for human artery walls, Journal of Biomechanics, Vol. 6, (1970), 13-24.

35. N. Westerhof, A. Noordergraaf, Arteral Viscoelasticity: A generalized model, Journal of Biomechanics, Vol. 3, (1970), 357-379.

36. G. E. Saito, T. J. Vander Werff, The importance of viscoelasticity in arterial blood flow model, Journal of Biomechanics, Vol. 8, (1975), 237-245.

37. W. R. Milnor, Hemodynamics, 2nd edition, Williams and Wilkins, Baltimore and London, 1989.

38. W. J. A. Goedhard, A. A. Knoop, A model of the artery wall, Journal of Biomechanics, Vol. 6, (1973), pp 281-288.

39. B. S. Gow, M. G. Taylor, Measurement of viscoelastic properties of arteries in

living dogs., Circulation Research, Vol. 23, (1968), pp. 111-122.

40. B. M. Learoyd, M. G. Taylor, Alterations with age in the viscoelastic properties of human artery walls, Circulation Research, Vol. 18, (1966), pp. 278-292.

41. T. Yamaguchi, T. Nakayama and T. Kobayashi, Computations of the wall mechanical response under unsteady flows in arterial diseases, 1996 Advances in Bioengineering, BED-Vol. 33, (1996), pp. 396-370.

42. Y. G. Lai and A. J. Przekwas, A finite-volume method for fluid flow simulations with moving boundaries, J. Comp. Fluid Dyn., Vol. 2, (1996), pp. 19-402.

43. J. Wang, M. S. Gadala, Formulation and survey of ALE method in nonlinear solid mechanics, Finite Elements in Analysis and Design, Elsevier, Vol. 24, (1997), pp. 253-269.

44. T. Nomura, ALE finite element computations of fluid-structure interaction problems, Computer Methods in Applied Mechanics and Engineering, Vol. 112, (1994), pp. 291-308.

45. Y. N. Jeng and J. L. Chen, Geometric conservation law of the finite-volume method for the Simpler Algorithm and a proposed upwind scheme, Numerical Heat Transfer, Part B, Vol. 22, (1992), pp. 211-234.

46. Y. C. Fung, Biodynamic Circulation, Springer-Verlag, New York, Inc., 1984.

47. A. Iserles, A first course in the numerical analysis of Differential equations, Cambridge University Press, New York, 1996.